Aspects of the biological carbon cycle in a ca. 3.42-billion-year-old marine ecosystem

M. Reinhardt [a,b,*], V. Thiel [a], J.-P. Duda [a], A. Hofmann [c], D. Bajnai [d], W. Goetz [e], A. Pack [d], J. Reitner [a], M. Schanofski [f], J. Schönig [g], M.J. Whitehouse [h], H. Drake [b]

[a] University of Göttingen, Department of Geobiology, 37077, Göttingen, Germany
[b] Linnæus University, Department of Biology and Environmental Science, 39182, Kalmar, Sweden
[c] University of Johannesburg, Department of Geology, Johannesburg 2006, South Africa
[d] University of Göttingen, Department of Geochemistry and Isotope Geology, 37077, Göttingen, Germany
[e] Max Planck Institute for Solar System Research, Planetary Science Department, 37077, Göttingen, Germany
[f] University of Göttingen, Department of Mineralogy, 37077, Göttingen, Germany
[g] University of Göttingen, Department of Sedimentology, 37077, Göttingen, Germany
[h] Swedish Museum of Natural History, 10405, Stockholm, Sweden

ARTICLE INFO

ABSTRACT

Microbial life on Earth was well established in the Paleoarchean, but insight into early ecosystem diversity and thus, the complexity of the early biological carbon cycle is limited. Here we investigated four carbonaceous chert samples from the lower platform facies of the ca. 3.42-billion-year-old Buck Reef Chert, Barberton greenstone belt. The analysis on multiple scales revealed exceptionally well-preserved carbonaceous matter, even on molecular level (aliphatic and aromatic hydrocarbons), resulting from rapid silicification. Geochemical evidence from stable carbon and multiple sulfur isotopes supports the presence of different microbial metabolisms in the Paleoarchean ecosystem. The local biological carbon cycle was dominated by photoautotrophs, but autotrophic sulfate reducers and methane- or acetate-producing microbes were also present. In areas of microbial methane or acetate release, methanotrophs or acetotrophs contributed to the overall biomass. These results highlight the metabolic diversity in the lower platform environment of the Buck Reef Chert, and underline that an advanced biological carbon cycle already existed in the early Archean.

1. Introduction

In the Paleoarchean Era (3.6–3.2 Ga), microbial life was already well established on Earth. Early microbial fingerprints can be found in marine, hydrothermal, and cryptic environments (Cavalazzi et al., 2021; Djokic et al., 2017; Duda et al., 2018; Hickman-Lewis et al., 2018; Philippot et al., 2007; Tice and Lowe, 2004; Ueno et al., 2006). Rather complex microbial ecosystems probably existed in some settings, involving metabolisms using light or chemical energy sources (Hickman-Lewis et al., 2020b; Morag et al., 2016; Westall et al., 2011). However, it is challenging to assess the diversity of early microbial ecosystems in detail, as the oldest geological archives on Earth, including potential biosignatures, are only rarely preserved due to constant recycling of the Earth's crust. The information to reconstruct early ecosystems generally comes from morphological and geochemical fingerprints (Hickman-Lewis et al., 2018; Hickman-Lewis et al., 2020a; Lepot, 2020; Philippot et al., 2007; Tice and Lowe, 2004; Wacey et al., 2010; Walsh and Lowe, 1985), but the combination of several potential bio-indicators is required as many biosignatures can also be mimicked by abiotic processes (Brasier et al., 2002; McCollom and Seewald, 2006; McMahon, 2019).

In this study, we provide multiple lines of evidence to support microbial diversity in a Paleoarchean environment from the lower platform facies of the 3.42 Ga old Buck Reef Chert, Barberton greenstone belt, South Africa. The Barberton greenstone belt contains several sedimentary units that preserved diverse biosignatures of early life (Homann, 2019), including the carbonaceous remains of primeval microorganisms (Cavalazzi et al., 2021; Hickman-Lewis et al., 2018; Tice and Lowe, 2004; van Zuilen et al., 2007; Walsh and Lowe, 1985; Westall et al., 2011). Particularly the Buck Reef Chert, the basal member of the

---

Kromberg Formation, Onverwacht Group, represents one of the best-preserved sedimentary records of Paleoarchean life, including morphological and geochemical traces of anoxygenic phototrophs, anaerobic ammonium oxidizers, and potentially methane cycling microbes (Pellerin et al., 2023; Tice, 2009; Tice and Lowe, 2004, 2006b; Walsh and Lowe, 1985). The sediments accumulated on a subsiding volcanic platform, in part as primary precipitates from Archean seawater (Ledevin et al., 2019; Lowe and Knauth, 1977; Stefurak et al., 2014, 2015), and are attributed to three different depositional facies, i. e., evaporitic, platform, and deep basin facies (Hofmann and Bolhar, 2007; Lowe and Fisher Worrell, 1999; Tice and Lowe, 2004). Carbonaceous matter (CM) is abundant in various chert types and has been subjected to lower greenschist grade metamorphism (Alleon et al., 2021;

Greco et al., 2018; Hofmann et al., 2013a; Tice et al., 2004; van Zuilen et al., 2007). The CM occurs either in microbial mat structures or as detrital particles in sedimentary layers (Ledevin et al., 2019; Lowe, 1999; Lowe and Knauth, 1977; Tice, 2009; Tice and Lowe, 2004; Walsh and Lowe, 1999). Synsedimentary silicification caused rapid induration of some of the carbonaceous cherts (Hofmann et al., 2013a; Ledevin et al., 2019; Lowe, 1999; Lowe and Knauth, 1977; Stefurak et al., 2014; Walsh and Lowe, 1999), promoting the spectacular preservation of (carbonaceous) microbial mat structures.

Here we report on CM in lower platform black-and-white banded cherts and black massive chert (Fig. 1), entrapped in microbial laminations or inside the silica matrix, sometimes in association with pyrite and siderite. Various macro- and micro-scale analytical techniques were
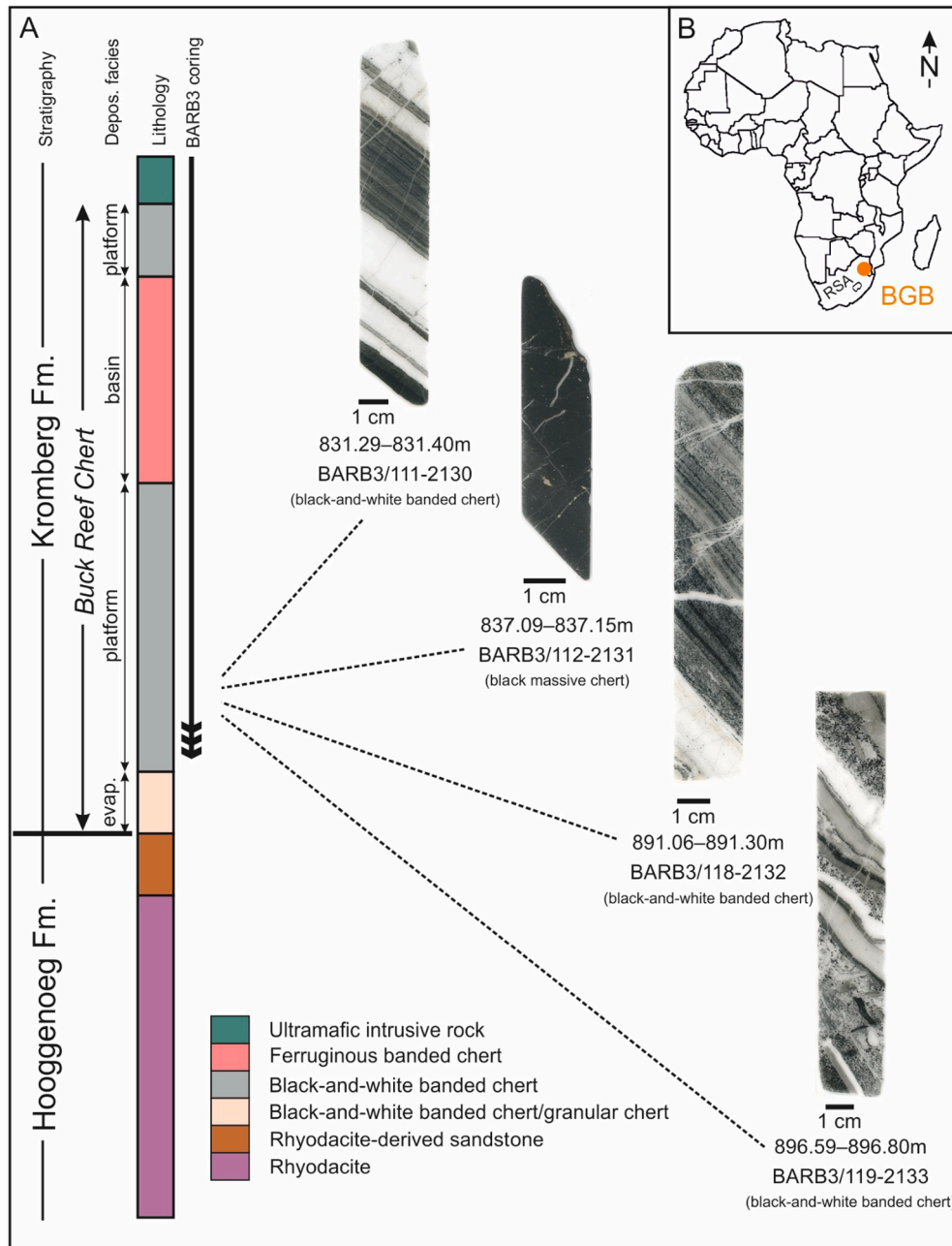

Fig. 1. Sampling location and stratigraphy. A, Stratigraphic overview of the contact between the Hooggenoeg and Kromberg formations (modified after Greco et al., 2018). The Buck Reef Chert is a sedimentary sequence marking the base of the Kromberg Formation, and has a thickness of 250–400 m (Homann, 2019; Lowe and Fisher Worrell, 1999). The chert succession overlies volcanic rhyodacite and its erosion products, and is capped by an ultramafic sill (Hofmann et al., 2013b). The BARB3 drill core reaches into the lowermost part of the lower platform facies. The four cherts investigated were sampled from an interval of ca. 66 m, between 831 and 897 m depth. B, Map showing the location of the Barberton greenstone belt (BGB) in the northeast of the Republic of South Africa (RSA).

combined to provide information on microbial activity in the ancient environment. Stable carbon isotope analyses support the dominance of photoautotrophs in the lower platform ecosystem, but chemoautotrophic sulfate reducers, methanogens and/or acetogens (including their metabolic counterparts) were probably also present. Thus, the local ecosystem 3.42 Ga ago, in which the chert precursors formed, was likely driven by a considerable diversity of microbial metabolisms.

2. Material and methods

2.1. Sample material

Four chert samples of the ca. 3.42 Ga Buck Reef Chert were investigated, covering a ca. 66 m interval of the lower platform facies (Fig. 1). The latter includes two lithofacies, namely lower and upper black-and-white banded chert, which are characterized by alternating layers of white pure chert (ca. 0.1–10 cm thick) and black carbonaceous chert (<1–15 cm thick) (Tice and Lowe, 2004, 2006b). Plastic deformation and disruption of white bands, stratiform cavity fillings of mega-quartz, and layers with sand-sized carbonaceous particles characterize the lower black-and-white banded chert. In the upper black-and-white banded chert, deformation features are rare, carbonaceous matter appears in finely laminated layers, and the ferruginous character is increasing (Tice and Lowe, 2006b). The studied samples cover both lithofacies (lower black-and-white banded chert, BARB3/119–2132 and BARB3/118–2133; upper black-and-white banded chert, BARB3/111–2130 and BARB3/112–2131), while one sample consist only of black massive chert without white chert bands (BARB3/112–2131).

The samples were recovered during the Barberton Drilling Project from drill core BARB3 (Hofmann et al., 2013b), and the core was stored in stainless-steel boxes under dry conditions in the core repository at the University of Johannesburg, Republic of South Africa. The samples were selected based on visual inspection of CM abundance and the appearance of CM in microbial mat structures. Quarters of the selected core sections (multiple centimeter-sized pieces; Fig. 1, and Fig. S1A) were cut with a pre-cleaned rock saw at the University of Johannesburg and wrapped into clean laboratory aluminum foil (Carl Roth; see aluminum foil blank Fig. S2A) for shipping to the Göttingen laboratory, where the samples were processed further.

2.2. Microscopy

A Zeiss SteREO Discovery.V8 stereomicroscope connected to an AxioCam MRc5 5-megapixel camera and an Olympus BX53M polarization microscope were used for transmitted and reflected light microscopy. Chert fragments were investigated using a Hitachi S-3400 N Scanning Electron Microscope (SEM) equipped with an integrated EDS system and an environmental SEM (ESEM) with a FEI QUANTA FEG 650 (Oxford Instruments, UK) EDS and an Oxford T-Max 80 detector.

2.3. Bulk geochemical analyses

Total organic carbon (TOC) and total inorganic carbon (TIC) of the cherts were analyzed with a Leco RC612 temperature-programmable carbon analyzer. Element distributions, including K, Si, and Fe, were measured on sample slices using a Bruker M4 Tornado micro X-ray fluorescence (μ-XRF) scanner equipped with a rhodium target X-ray tube at 50 kV and 200 μA. The H/C ratios of extracted CM were determined from combustion elemental analysis of the CM via an Elementar MICRO cube elemental analyzer. The H/C ratio determination of BARB3/112–2131 CM was influenced by insoluble hydroxyfluorides (neoformation after phyllosilicate dissolution during HF treatment), increasing the H content of the CM concentrate. The bulk $^{13}C/^{12}C$ ratio of CM was analysed using a Flash 2000 elemental analyzer coupled to a Delta plus XP isotope ratio mass spectrometer via a ConFlo III interface (all instruments Thermo Fisher).

Stable carbon and oxygen isotope compositions of bulk carbonate (here siderite) in BARB3/111–2130, BARB3/118–2132 (including bulk siderite of a layer containing low-δ^{13}C-CM) and BARB3/119–2133 were determined using a Kiel-IV in combination with an isotope ratio mass spectrometer. The phosphoric acid digestion of the carbonates was done at 70 °C in a Thermo Kiel-IV carbonate preparation device. The resulting CO_2 analyte was analyzed on a Finnigan Delta Plus gas source isotope ratio mass spectrometer. The measured δ^{13}C and δ^{18}O values of two calcite standards (NBS-18: $\delta^{13}C_{carb} = -5.014$ ‰ VPDB, $\delta^{18}O = 7.00$ ‰ VSMOW; and IAEA-603: $\delta^{13}C_{carb} = 2.46$ ‰ VPDB, $\delta^{18}O = 28.48$ ‰ VSMOW) were compared to their accepted values, and the resulting differences were utilized to correct the sample data. The reproducibility of the measurements is 0.1 ‰ for $\delta^{13}C_{carb}$ and 0.2 % for δ^{18}O. To account for the difference in the acid fractionation factors between calcite and siderite, the normalized δ^{18}O values of the samples were additionally corrected by -1.25 ‰ ($=10^3\ln\alpha^{18}_{CO2(acid)/siderite} - 10^3\ln\alpha^{18}_{CO2(acid)/calcite}$ at 70 °C (Fernandez et al., 2016)).

2.4. Raman spectroscopy

Raman spectroscopy was conducted on single CM particles in thin sections of the drill core samples using a WITec alpha300 instrument, following the analytical settings and calibration reported in (Reinhardt et al., 2019). Spectra evaluation, including smoothing, baseline correction, and fitting, was performed with the WITec Control and Project software.

To map CM in secondary veins, two-dimensional Raman spectral images were collected using a WITec alpha300R fibre-coupled ultrahigh throughput spectrometer. Before analysis, the system was calibrated using an integrated light source. The experimental setup included a 532 nm excitation laser, an automatically controlled laser power of 20 mW, a 300 g × mm^{-1} grating, and a 100 × long working distance objective with a numerical aperture of 0.75. The setup has a spectral resolution of ∼ 2.2 cm^{-1}. Spectra were collected at a step size of 1 μm in horizontal and vertical direction by an acquisition time of 50 ms for each spectrum. The short acquisition time enabled the detection of sensible low-temperature CM at the comparatively high laser power of 20 mW (Fig. S3). Automated cosmic ray correction, background subtraction, and component analysis were performed using the WITec Project software.

We applied 4-Voigt-function and 5-Voigt-function fitting procedures to all CM spectra. Band nomenclature for the 4-Voigt fitting (D1, D3, G, and D2) follows Beyssac et al., 2002. Band nomenclature for the 5-Voigt fitting (D4, D1, D3, G, and D2) follows Sforna et al., 2014. For metamorphic temperature calculation the Raman geothermometer based on the R2 ratio (R2 = D1/(G + D1 + D2)) after Beyssac et al., 2002 was used (uncertainty of ± 50 °C).

2.5. Fourier transform infrared spectroscopy-attenuated total reflection

Fourier transform infrared spectroscopy-attenuated total reflection (FTIR-ATR) spectra were acquired on a Bruker Vertex 70 FTIR spectrometer. Isolated and extracted CM was analyzed in a spectral region of 4000–400 cm^{-1} with the equipped diamond-ATR unit. Measurements were conducted using a Globar light source, a KBr beam splitter, a 6 mm aperture, and a RT-DLATGS Wide-Range detector. 128 scans per measurement with a spectral resolution of 4 cm^{-1} were collected. The intensities of the single-beam spectra of the samples (I) were ratioed against the intensity of a single-beam background spectrum of air (I_0) to obtain spectra in absorbance units ($-\log_{10}(I/I_0)$). A synthetic graphite and a natural pyrobitumen (Fennoscandian shield, Sweden) have been analyzed subsequently for comparison.

2.6. Secondary ion mass spectrometry

Chert fragments containing CM and pyrite, and loose pyrite crystals
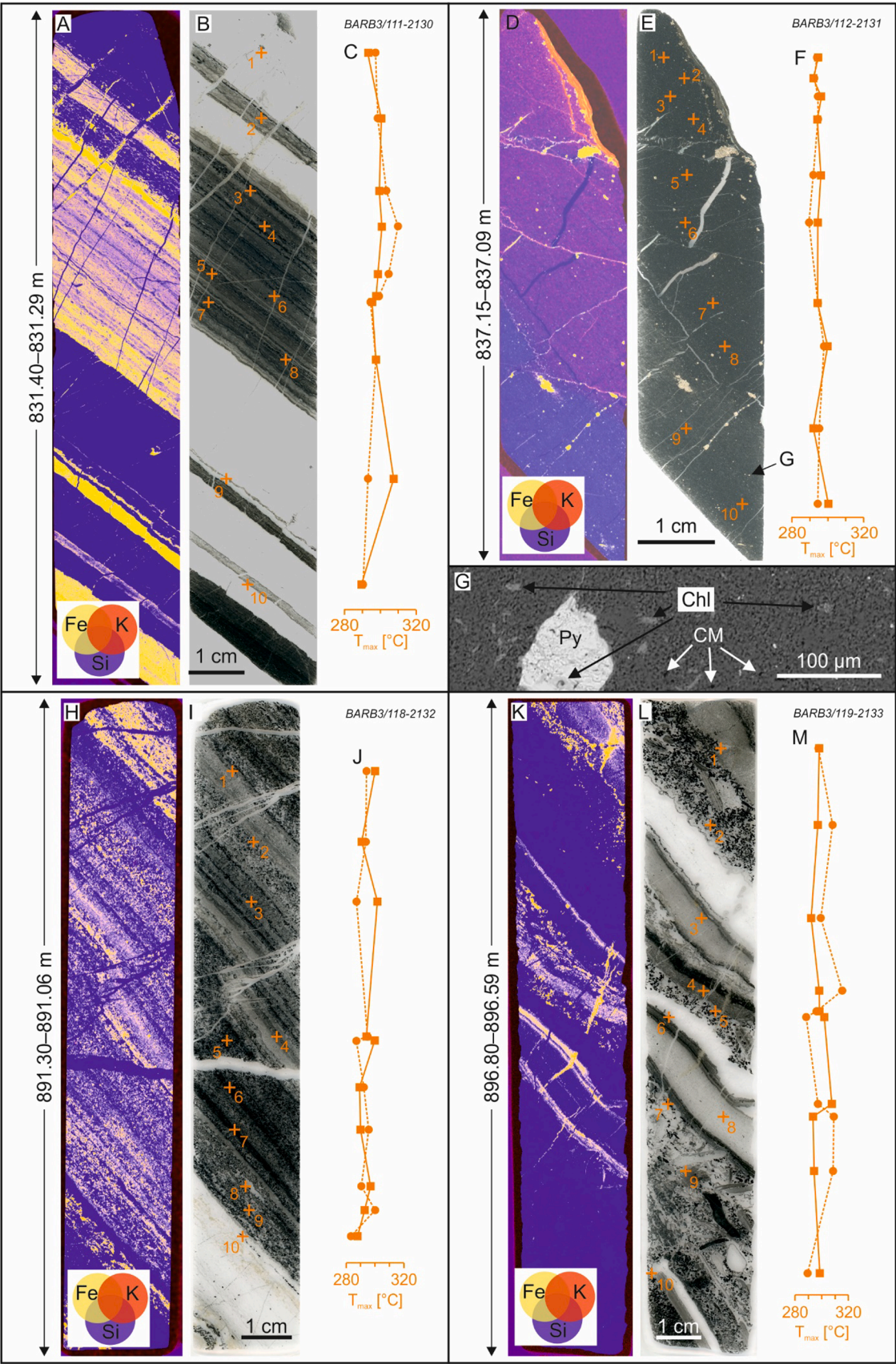
(caption on next page)

Fig. 2. **Petrographic overview and Raman temperatures of carbonaceous matter (CM) in Buck Reef Cherts samples.** A, H, K, Micro X-ray fluorescence (μ-XRF) scans of the black-and-white banded chert samples, showing distributions of silicon (blue), iron (yellow), and potassium (red). Here, iron is mainly associated with siderite. D, μ-XRF scan of the black massive chert sample, showing distributions of silicon (blue), iron (yellow), and potassium (red). Here, iron is mainly associated with pyrite. Potassium is associated with sericite that is abundantly present in the silica matrix (magenta). B, I, L, Transmitted light microscopic images of the black-and-white banded chert samples, showing alternating layers consisting of pure silica (white) and silica plus siderite (grey) with CM (black) in microbial mat structures. Numbered orange crosses mark the CM particles analyzed by Raman spectroscopy. E, Transmitted light microscopic image of the black massive chert sample, showing finely distributed CM (black) in the phyllosilicate-rich silica matrix. Numbered orange crosses mark the CM particles analyzed by Raman spectroscopy. C, F, J, M, Raman temperature profiles based on a 4-Voigt-function (dashed line with filled circles) and a 5-Voigt-function fitting procedure (solid line with filled squares). T_{max} was calculated after Beyssac et al., 2002. G, Scanning electron microscope image from the black massive chert sample (exact location is marked in E), showing chlorite (Chl), pyrite (Py) and CM in microcrystalline silica. (For interpretation of the references to colour in this figure legend, the reader is referred to the web version of this article.)

were mounted in epoxy and polished to expose cross-sections. The pyrite crystals were examined with SEM to trace zonation and impurities prior to secondary ion mass spectrometry (SIMS) analysis. SIMS-analyses (10 μm lateral beam dimension, 1–2 μm depth dimension) of carbon isotopes in CM ($\delta^{13}C_{V\text{-}PDB}$), and multiple sulfur isotopes in pyrite ($\delta^{33}S_{V\text{-}CDT}$, $\delta^{34}S_{V\text{-}CDT}$, and $\Delta^{33}S$ (=$\delta^{33}S - 1000((1 + \delta^{34}S/1000)^{0.515} - 1)$)) were performed at the Swedish Museum of Natural History, Stockholm (NordSIM facility).

Multiple S isotope compositions (pyrites in BARB3/111–2130, BARB3/112–2131, BARB3/118/2132) were measured using a CAMECA IMS1280 instrument following the settings described in Whitehouse, 2013. The system was calibrated against the non-MIF Ruttan pyrite (n = 41) and Balmat pyrite (n = 20) standards (Crowe and Vaughan, 1966) (values redetermined by Cabral et al., 2013), with Ruttan pyrite as the primary $\delta^{34}S$ reference (assumed $\delta^{34}S = 1.41$ ‰, reproducibility 0.07 ‰, SD), and both defining the mass dependent fractionation line ($\Delta^{33}S$ reproducibility 0.14 ‰, SD on both standards). Two additional pyrite reference materials were analyzed as monitors: S0302A (n = 14), which yielded $\delta^{34}S = -0.01 \pm 0.10$ ‰, SD, in agreement with Magnall et al., 2016 and $\Delta^{33}S = -0.28 \pm 0.10$ ‰, SD (not previously characterized), and Isua 248,474 MIF pyrite (n = 11), which yielded $\delta^{34}S = 2.40 \pm 0.10$ ‰, SD and $\Delta^{33}S = 2.74 \pm 0.50$ ‰, SD. The latter value shows slightly higher dispersion than noted in other grains from this material, suggesting some heterogeneity in the mass independent signature, but within the error of the value reported by Whitehouse, 2013.

Analyses of $^{13}C/^{12}C$ ratios (CM in BARB3/111–2130 and BARB3/118–2132) were performed using the same CAMECA IMS1280 instrument as for the triple S isotope analyses. Instrument settings closely resemble those described in Hickman-Lewis et al., 2020a, comprising multicollection at mass resolutions of 2460 (^{12}C channel) and 4000 (^{13}C channel), with the exception that the ^{13}C channel utilized a Faraday detector instead of an ion counter in order to measure signals potentially in excess of ca. 1×10^6 cps (up to ca. 4×10^6 cps was obtained from the reference graphite and some targets; the latter varied substantially, with maximum cps up to 90 % of the reference material). Instrumental mass bias was determined using replicate analyses of an in house pyrolyzed graphite reference material (C-pyr2; $\delta^{13}C_{org} = -35.7 \pm 0.3$ ‰ cross calibrated against another pyrolyzed graphite C-pyr1 with $\delta^{13}C_{org} = -30.8$ ‰ (Nemchin et al., 2008)) and reproducibility of ca. 0.25 ‰ (SD) was obtained in two sessions. A previous study of organic carbonaceous material has shown that graphite is ca. 4 ‰ too light when calibrated against a carbon bearing chert reference material that yields unbiased values for CM (House et al., 2000). Hence it is expected that the values for organic material calibrated against graphite herein may be similarly light once the instrumental mass bias is corrected using the known composition of the graphite.

A matrix effect dependent on H/C ratio can cause instrumental mass fractionation of carbon isotopes during $\delta^{13}C$ analysis of CM via SIMS by up to 5 ‰ (Sangély et al., 2005). To correct for this instrumental fractionation, we analyzed two pyrobitumen reference materials from Kallmora and Grängesberg, Sweden, with known H/C (from Welin, 1966) and $\delta^{13}C_{org}$ composition (-30.1 ± 0.2 ‰ and -29.1 ± 0.2 ‰; analyzed on the same device as the chert CM) and applied H/C values of our samples. They were then used together with raw SIMS data to

determine the Δ_{inst} values for the effects of the elemental H/C-composition during $\delta^{13}C_{org}$ measurements, assuming the same linear behavior as in (Sangély et al., 2005). The Δ_{inst} and H/C ratio of the pyrobitumens, graphites and carbonaceous matter from the samples were then used to obtain session specific H/C-corrected $\delta^{13}C_{org}$ values, which were up to 1 ‰ heavier than the uncorrected values for sample BARB3/111–2130 and 0.85–0.86 ‰ heavier for sample BARB3/118–2132 that had lower H/C ratio. The reported 2σ estimates represent the analytical error. Epoxy contamination in the analysis was avoided by careful spot placement and detailed SEM documentation prior to spot placement.

2.7. Organic geochemical preparation

All organic solvents were distilled and tested for contamination with gas chromatography–mass spectrometry (GC–MS) before use. Glassware was heated to 550 °C for 4 h. Blanks were processed regularly (graphite, heated at 600 °C for 12 h, was processed in parallel to track a potential introduction of contaminants; Fig. S2B). Before solvent extraction, exteriors (2–5 mm) of the core samples were cut off (Fig. S1B) using a Buehler IsoMet 1000 precision saw. The saw blade was rigorously cleaned with organic solvents. The Millipore water used to cool the saw blade was extracted with dichloromethane (DCM) before use. A brick, heated at 600 °C for 12 h, was used to check for cleanliness of the sawing process (Fig. S2C). Fresh surfaces of the inner blocks were thoroughly cleaned with DCM. Both, the offcuts and inner blocks were grinded (Retsch MM 301 pebble mill; see pebble mill blank, Fig. S2D) and separately extracted. The offcuts that were in contact with the drill bit during coring or with the rock saw in Johannesburg were not used for kerogen isolation.

The soluble fraction of the CM (bitumen/oil, i.e., mobile in rocks) was recovered by ultrasonic extraction with DCM/methanol (3 + 1, *v/v*), DCM, and *n*-hexane. The mineral matrix of the residues was removed with HCl (37 %, 1 d, 20 °C) and HF (48 %, 7 d, 20 °C) (Durand, 1980). The remaining CM concentrates, including pyrite (insoluble in HCl and HF), were further purified by density separation using (i) a ZnBr solution (Love, 1982), and (ii) washing in a combination of methanol and *n*-hexane in a separating funnel (Fig. S1C). Methanol and *n*-hexane do not mix, and the different polarity of the solvents leads to CM accumulation on the methanol–*n*-hexane interface, while mineral particles sink down and can be drained through the funnel outlet. CM from BARB3/112–2131, however, still contained few fluorides and hydroxyfluorides after density separation that formed during HF treatment.

Purified CM was chemically cleaned by extensive extraction, and by swelling in pyridine (Brocks et al., 2003; Marshall et al., 2007), which allows for a rigorous removal of potentially attached bitumen that has not been removed during the previous extraction steps. In brief, CM was ultrasonically extracted with DCM (3x for 10 min at 20 °C), and *n*-hexane (3x for 10 min at 20 °C). Afterwards, CM was swelled in pyridine (2x for 2 h at 80 °C), and additionally extracted with methanol (10 min at 20 °C), DCM (3x 10 min at 20 °C), and *n*-hexane (10 min at 20 °C). The last extraction step was repeated until no soluble compounds were detected with GC–MS ('last solvent extract' in Fig. S4).

2.8. Catalytic hydropyrolysis

Isolated and chemically cleaned CM (Fig. S1D) included the actual insoluble macromolecular fraction of organic matter (inherently immobile) plus the non-soluble part of pyrobitumen (once mobile). The CM was pyrolyzed using catalytic hydropyrolysis (HyPy), an open system pyrolysis technique known for its high yields and minor alteration of cracking products (Love et al., 1995). Stimulated by the presence of a dispersed sulfided molybdenum catalyst (ammonium dioxydithiomolybdate, $(NH_4)_2MoO_2S_2$), moieties originally interlinked in macromolecules are released and hydrogenated through progressive heating in a permanent hydrogen atmosphere (150 bar) (Love et al., 1995).

Experiments were conducted with a Strata Technology Ltd. (Nottingham, UK) HyPy rig. Between 14.2 and 71.8 mg of catalyst-loaded CM was pyrolyzed. The permanent H_2 flow was set at 6 L min^{-1}. In a stepwise heating approach, the CM was first thermally cleaned (release of potential residual bitumen or other non-bound organic components, e.g., modern contaminants that were trapped inside the dense macromolecular network and not released during extensive solvent extraction) by heating from ambient temperature to 250 °C (at 300 °C min^{-1}) and then to 330 °C (at 8 °C min^{-1}, held for 10 min). In a next step, CM macromolecules were pyrolyzed by heating from ambient temperature to 520 °C (at 8 °C min^{-1}), releasing solely covalently bound moieties. The products from the 330 °C and the 520 °C runs were sampled separately in a dry ice-cooled silica gel trap (Meredith et al., 2004). The trapped molecules were recovered from the silica using DCM. HyPy rig blank and catalyst blank runs were conducted before each sample. Two CM portions from BARB3/112–2131 were pyrolyzed to ensure reproducibility of the pyrolysis result.

2.9. Gas chromatography–Mass spectrometry

Molecular compositions from extracts and hydropyrolysates were analyzed with a Thermo Trace 1310 gas chromatograph (GC) coupled to a Thermo TSQ Quantum Ultra triple quadrupole mass spectrometer (MS). The GC had a Phenomenex Zebron ZB-5MS fused silica capillary column (30 m length, 0.25 mm internal diameter, 0.25 μm film thickness). Samples were injected with a Thermo TriPlus RSH autosampler into a splitless injector and transferred to the GC column at 300 °C. The helium flow rate was set at 1.5 mL min^{-1}. The GC oven was programmed from 80 °C (held for 1 min) to 310 °C (held for 30 min, heating rate 5 °C min^{-1}). The MS source was operated in electron ionization mode at 240 °C and 70 eV. Organic compounds were analyzed in full scan mode (scan range 50–600 amu), and identified by comparison with published mass spectra and retention times. All samples were dissolved in a defined volume of 50 μL *n*-hexane prior to analysis, and an aliquot of 1 μL was analyzed.

2.10. Gas chromatography–Combustion–Isotope ratio mass spectrometry

Compound-specific stable carbon isotope ratios ($\delta^{13}C_{V-PDB}$) were analyzed on the 520 °C hydropyrolysates using a Trace GC coupled to a Delta C isotope ratio mass spectrometer via a GC combustion interface (all instruments Thermo Finnigan). The chromatographic conditions were similar to the TSQ analyses (GC–MS), except that an Agilent DB5-MS column and a split/splitless injector was used (300 °C, splitless time 0.8 min). The combustion reactor was set to 940 °C. The instrumental bias was determined by analyzing *n*-icosane of known isotopic composition ($\Delta_{real-measured} = -0.4$ ‰), and the $\delta^{13}C$ of individual compounds was corrected accordingly.

3. Results

3.1. Petrography and geochemistry

We analyzed black-and-white banded chert (samples BARB3/ 111–2130, BARB3/118–2132 and BARB3/119–2133) and black massive chert (BARB3/112–2131) from the lower platform facies of the Buck Reef Chert (Fig. 1). The black-and-white banded cherts mainly consist of quartz, CM, siderite, and little pyrite (Fig. 2A, H, K, Fig. 3A–F, and Fig. S5A, C, D). Silica granules appear in some layers (Fig. 3A, B, and Fig. S5A, C). Iron oxides are not present. Single siderite crystals can be as large as 500 μm (Fig. 3D, G). Bulk $\delta^{13}C_{carb}$ of the siderite varies from -3.7 ± 0.1 ‰ to -1.3 ± 0.1 ‰ and $\delta^{18}O$ from 15.9 ± 0.2 ‰ to 17.1 ± 0.2 ‰ (Table 1). In the black-and-white banded cherts, CM-rich sequences alternate with CM-lean sequences (single carbonaceous layers up to a few millimeters thick; Fig. 2B, I, L, and Fig. S5A, C, D). The TOC ranges between 0.08 and 0.14 wt%, and the TIC ranges between 0.54 and 2.86 wt% (Table 1). CM appears as non-compacted lumps and sub-spherical particles with diameters up to 500 μm in sedimentary layers composed of pure silica or silica and siderite (Fig. 3A–F, and Fig. S5A, C, D). Furthermore, CM makes up laminae that may anastomose and drape the underlying sediment (Fig. 3A–D, and Fig. S5A, C). Some of these laminae are disrupted and show roll-up structures (Fig. 3F). In BARB3/119–2133 re-worked clasts of CM-rich chert in a silica matrix are present in some layers (Fig. 2L, Fig. 3E, Fig. S5D).

The black massive chert mainly consist of phyllosilicates, quartz, CM, and pyrite (Fig. 2D, G, and Fig. S5B). The TOC content is 0.49 wt% and the TIC content is 0.23 wt% (Table 1). Fine CM particles with a size $\leq$ 500 μm are homogenously distributed in the phyllosilicate-rich microcrystalline silica matrix over the whole 6 cm thick sample (Fig. 2D, G, and Fig. S5B). Unlike the black-and-white banded cherts, white chert bands and distinct continuous carbonaceous laminae are absent (Fig. S5B).

Most of the CM in the chert samples is preserved in sedimentary layers. However, secondary veins also contain minor CM (Fig. 3H, I, and Fig. S6). Those veins mainly consist of quartz, but may contain siderite and pyrite (Fig. S6). In BARB3/118–2132, CM occurs in blocky shape in a quartz vein oriented parallel to the sedimentation plane (Fig. 3H, I).

CM of the black-and-white banded cherts shows H/C ratios ≤ 0.15 (Table 1). The H/C ratio of black massive chert CM is 0.35, but may be overestimated due to hydrogen introduction from incomplete removal of hydroxyfluorides formed during HF treatment (see section 2.7).

The $\delta^{13}C_{org}$ values of bulk CM in the cherts studied range from -32.4 ± 0.2 to -28.3 ± 0.2 ‰ (Table 1). Microscale SIMS analysis of individual CM particles associated with sedimentary pyrite and siderite reveals even lower values. For instance, pyrite-associated CM in BARB3/ 111–2130 reveals $\delta^{13}C_{org}$ values between -36.6 ± 0.3 ‰ and -39.9 ± 0.3 ‰ (Fig. 4B, and Data S1), and siderite-associated CM in BARB3/ 118–2132 shows values as low as -44.0 ± 0.9 ‰ (Fig. 3G, and Data S1). In contrast, the CM with blocky shape from a vein of botryoidal chert with quartz in the center in BARB3/118–2132 shows micro-scale $\delta^{13}C_{org}$ values between -30.6 ± 0.3 ‰ and -33.0 ± 0.2 ‰ (Fig. 3J).

Pyrite is present in all cherts in different quantities (BARB3/ 112–2131 > BARB3/111–2130 > BARB3/118–2132 > BARB3/ 119–2133), and partly shows several growth generations. Pyrite cores (first generation) in the black-and-white banded cherts BARB3/ 111–2130 and BARB3/118–2132 contain quartz and CM inclusions (Fig. 4A, B). In the black massive chert BARB3/112–2131 the pyrite cores enclose sericite, chlorite and CM, and only later formed pyrite (second generation) contains quartz inclusions (Fig. 4C). Some pyrites from BARB3/112–2131 additionally have inclusion-free rims.

Single pyrite crystals were analyzed for multiple sulfur isotopes via SIMS (Fig. 5), including transects from the crystal core to the rim (Fig. 4A, B). Pyrite crystals from BARB3/112–2131 have $\delta^{34}S$ values ranging from 2.4 ± 0.2 ‰ to -5.4 ± 0.2 ‰, $\delta^{33}S$ between 1.9 ± 0.4 ‰ to -2.9 ± 0.3 ‰, and $\Delta^{33}S$ ranging from 0.7 ± 0.3 ‰ to -0.6 ± 0.2 ‰, with similar values for cores and veins, but higher $\delta^{34}S$ in rims (Fig. 4F, Fig. 5, and Data S1). Pyrite crystals from BARB3/111–2130 and BARB3/ 118–2132 possess $\delta^{34}S$ values between 3.3 ± 0.1 ‰ and -1.5 ± 0.1 ‰, $\delta^{33}S$ between 4.6 ± 0.4 ‰ to -0.5 ± 0.3 ‰, and $\Delta^{33}S$ values between 3.2 ± 0.3 ‰ and 0.1 ± 0.2 ‰. The latter two samples exhibit a notable
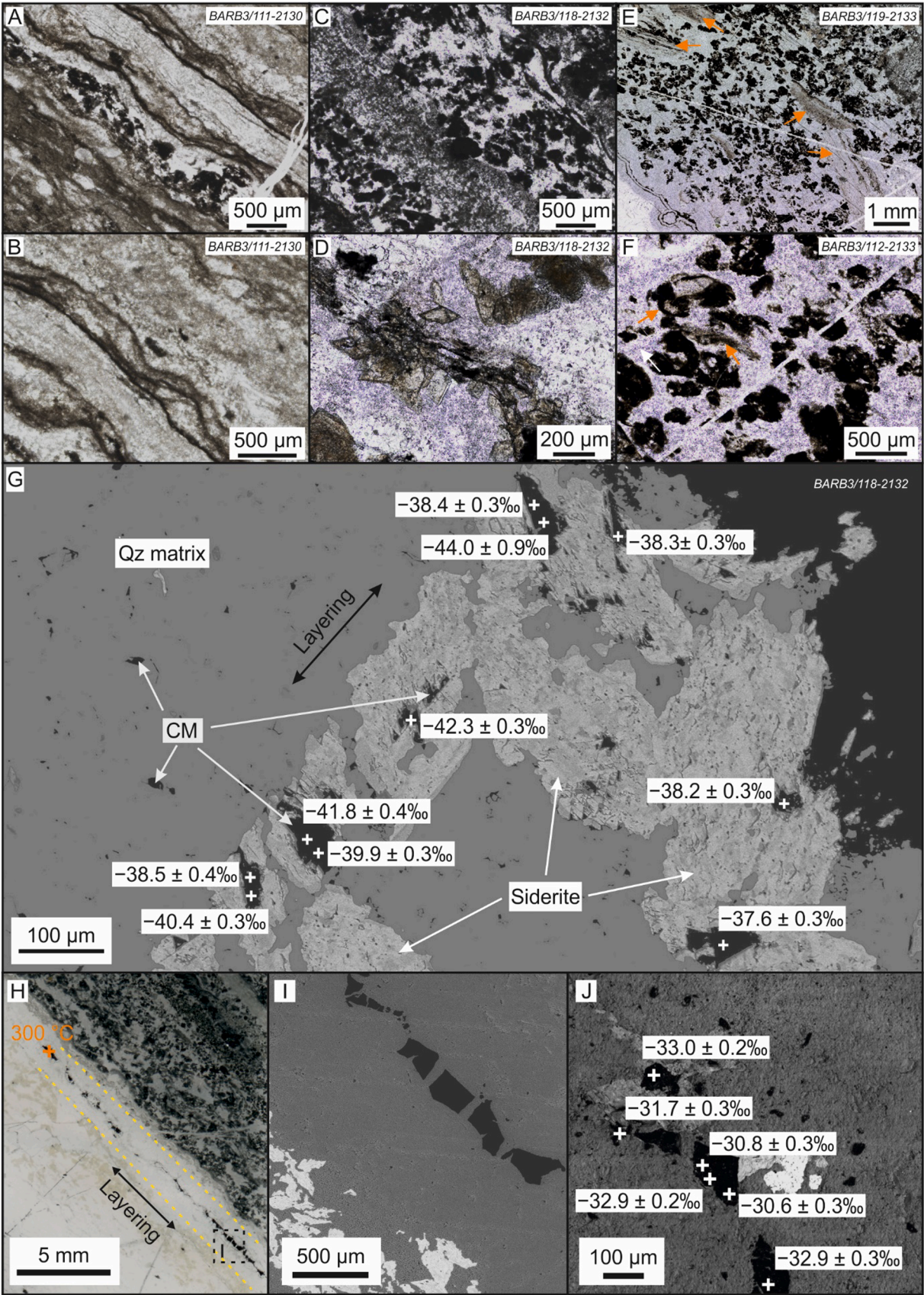
(caption on next page)

Fig. 3. Carbonaceous matter (CM) appearance in black-and-white banded chert. A–F, Transmitted light microscopic images from black-and-white banded chert (BARB3/111–2130, BARB3/118–2132, BARB3/119–2133). In black-and-white banded chert, CM (black) appears in laminae and anastomosing structures, draping the underlying sedimentary layers (A–D), and as roundish uncompacted detrital particles (A–F) enclosed in a microcrystalline silica matrix (white and grey areas; A–F). In some sedimentary layers, the CM is also associated with siderite (brownish areas; A, B, D) that partly forms euhedral crystals (D). Re-worked chert clasts with CM in laminae and/or as roundish particles occur in BARB3/119–2133 (orange arrows in E). In additon, disrupted microbial mat fragments appear in BARB3/119–2133 and are partly rolled up (orange arrows in F). G, Scanning electron microscope (SEM) image from BARB3/118–2132, resembling an area equivalent to (D). Here, CM partly appears together with siderite that shows two generations (two different shades of grey in the siderite accumulations). White crosses denote spots for $\delta^{13}C_{org}$ analysis via secondary ion mass spectrometry (SIMS). Errors of the $\delta^{13}C_{org}$ values are 2σ estimates (analytical error). H, Transmitted light microscopic image (BARB3/118–2132), showing a stratiform chert/quartz vein (marked by the yellow dashed lines) containing CM (black) in the center. The orange cross marks the spot for Raman spectroscopy analysis. Raman geothermometry revealed lower greenschist-facies overprint of ca. 300 °C (temperature calculated after Beyssac et al., 2002). The black square marked by dashed lines in the lower right corner denotes the area shown in (I). I, SEM image of the vein center, showing CM (black) with the characteristic blocky shape of pyrobitumen. J, Another SEM image of the pyrobitumen in BARB3/118–2132 (prolongation of the chert/quartz vein visible in H) including stable carbon isotope values measured via SIMS. White crosses mark the spots for analysis. Errors of the $\delta^{13}C_{org}$ values are 2σ estimates (analytical error). (For interpretation of the references to colour in this figure legend, the reader is referred to the web version of this article.)

Table 1

Bulk geochemical parameters.

Sample ID	Lithology	Chert sample				Siderite				Carbonaceous matter (CM)			
		TOC	± 2σ	TIC	± 2σ	$\delta^{13}C_{carb}$ [‰]	± 2σ	$\delta^{18}O$ [‰]	± 2σ	H/C	± 2σ	$\delta^{13}C_{org}$ [‰]	± 2σ
BARB3/ 111–2130	Black-and-white banded chert	0.09	0.01	2.86	0.02	−3.7	0.1	15.9	0.2	0.14	<0.01	−29.5	0.2
BARB3/ 112–2131	Black massive chert	0.49	<0.01	0.23	0.02	–	–	–	–	0.35*	0.01	−32.4	0.2
BARB3/ 118–2132	Black-and-white banded chert	0.14	0.01	1.98	0.02	−1.3	0.1	17.1	0.2	0.12	<0.01	−28.3	0.2
						−1.8†	0.1	16.3†	0.2				
BARB3/ 119–2133	Black-and-white banded chert	0.08	0.02	0.54	0.02	−2.3	0.1	16.7	0.2	0.15	<0.01	−31.0	0.2

All values represent mean values from duplicate analyses. TOC = total organic carbon, TIC = total inorganic carbon.

* includes H from neoformed hydroxyfluorides during HF treatment.

† siderite layer with isotopically light CM.

spatio-temporal trend of higher $\Delta^{33}S$ values in the crystal cores compared to the rims (Fig. 4D, Fig. 5, and Data S1). The $\delta^{34}S$ value trends show correspondence to different pyrite generations in some cases (increase of almost 3 ‰ with growth of the first generation, followed by a drop of 2 ‰ at the onset of the second generation; Fig. 4D).

3.2. Raman spectroscopy

Raman spectra of the CM particles, including CM in sedimentary layers and secondary veins show an intense D1 band at ca. 1354 cm^{-1} and a smaller G + D2 composite band at ca. 1608 cm^{-1} (Fig. S6, and Fig. S7) which is typical for disordered CM. Raman geothermometry estimates T_{max} to ca. 300 °C in all samples for both, 4-Voigt and 5-Voigt-fitting procedures (between 292 ± 21 °C and 300 ± 28 °C, respectively; Fig. 2C, F, J, M, and Table S1). T_{max} calculated from vein CM spectra ranges between 296 ± 21 °C and 326 ± 1 °C (Table S1).

3.3. Fourier transform infrared spectroscopy-attenuated total reflection

Infrared absorbance spectra of CM particles and synthetic graphite show an elevated baseline (moderate to strong background absorption). In the CM spectra, absorbance notably increases between 1000 and 700 cm^{-1} (Fig. S8), probably including aromatic C–H out-of-plain bending bands between 900 and 700 cm^{-1}. Another increase is observed between 600 and 450 cm^{-1}. Furthermore, weak C–H stretching bands of aliphatic components are visible at 2956 cm^{-1}, 2924 cm^{-1}, and 2851 cm^{-1} (Fig. S8).

3.4. Molecular composition of the exterior and interior solvent extracts

Solvent extracts from exterior and interior sample parts (contamination check) contain medium- to long-chain *n*-alkanes, with ≥ 14 carbons (Fig. S9, and Fig. S10). Total *n*-alkane concentrations in the exterior parts are partly higher than in the interiors, especially for

BARB3/111–2130 and BARB3/118–2132 (Fig. S10). BARB3/118–2132, for instance, shows 58.0 vs. 14.2 ng/g chert of total *n*-alkanes in exterior vs. interior extracts, while BARB3/119–2133 shows 15.7 vs. 25.0 ng/g chert of total *n*-alkanes in exterior vs. interior extracts (Table S2). Aromatic hydrocarbons were not observed in exterior and interior extracts (Fig. S9).

3.5. Molecular composition of the hydropyrolysates

The hydropyrolysis products of insoluble CM particles (i.e., excluding extractable molecules after organic-geochemical preparation) yielded a diversity of aliphatic and aromatic hydrocarbons. The 520 °C hydropyrolysates of CM prepared from the black-and-white banded cherts mainly contain *n*-alkanes and minor methyl-branched alkanes (C_{12}–C_{26}; Fig. S4A, C, D, and Fig. S11A, C, D). Total *n*-alkane concentrations range from 39.3 to 55.4 ng/g chert, corresponding to 39.6 to 68.9 μg/g TOC (Table S3). Highest amounts of *n*-alkanes were released from the CM of BARB3/119–2133 (Fig. 6). Moreover, various polycyclic aromatic hydrocarbons (PAHs) are also observed in all black-and-white banded chert hydropyrolysates (Fig. S4), but in lower abundances than the *n*-alkanes. The GC–MS runs of all studied cherts additionally showed a 'hump' of a complex compound mixture that could not be chromatographically resolved (Fig. S4).

The 520 °C hydropyrolysate of CM from the black massive chert (BARB3/112–2131) also contains *n*-alkanes and methyl-branched alkanes (C_{12}–C_{22}; Fig. S4B, and Fig. S11B), but has a stronger aromatic character, with PAHs being relatively more abundant as compared to the black-and-white banded cherts (Fig. S4). The total *n*-alkane concentration of this sample is 22.3 ng/g chert, which equals to 4.5 μg/g TOC (Table S3). It thus shows the lowest amounts of *n*-alkanes released from CM during pyrolysis (Fig. 6).

In addition, small amounts of pyrolytic *n*-alkenes appear in all 520 °C hydropyrolysates, with *n*-alk-1-enes being the most abundant (Fig. S12). The 330 °C HyPy runs (thermal cleaning), HyPy blanks and last solvent
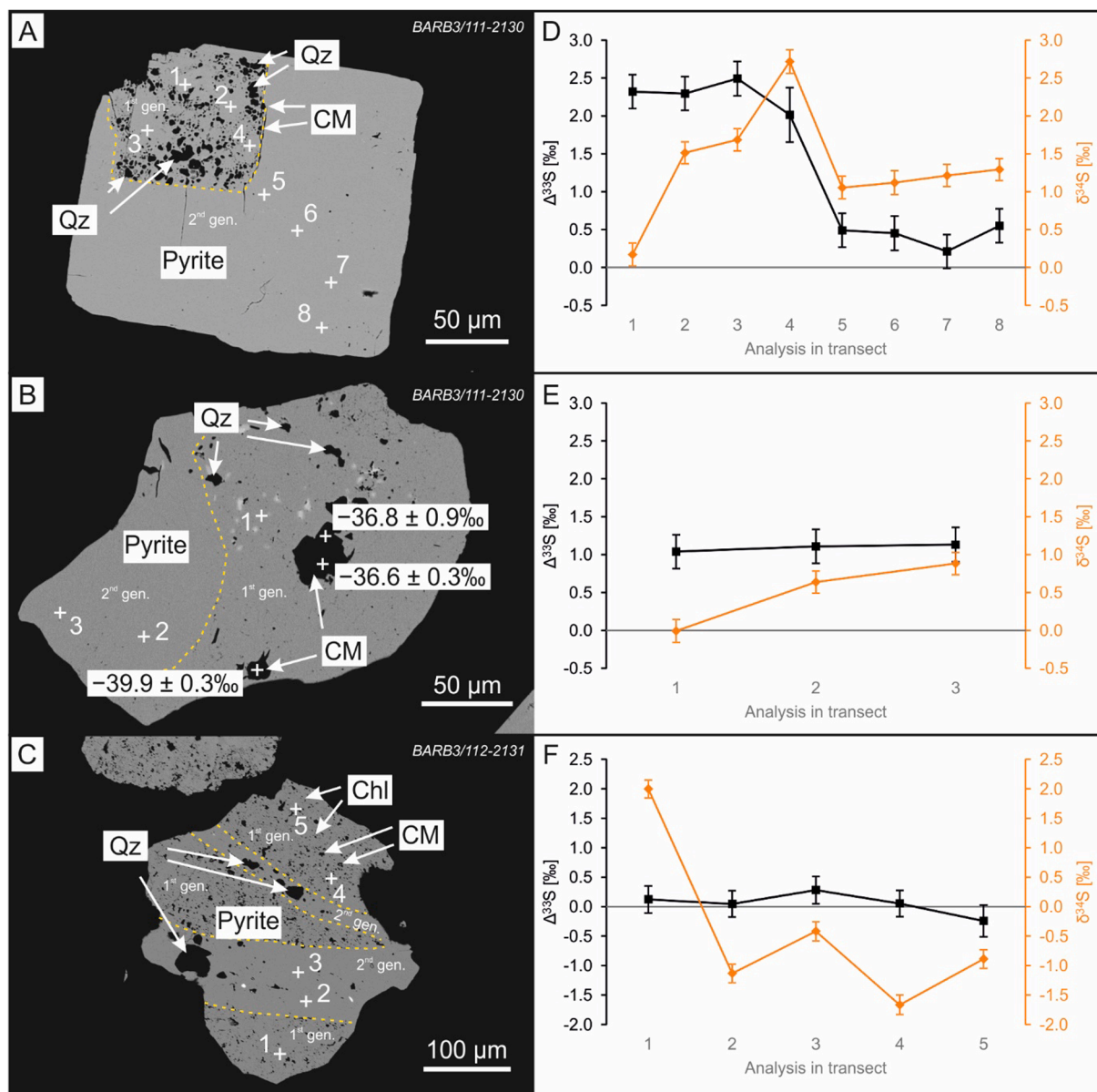
Fig. 4. Microscale sulfur isotope distribution in pyrite. A, B, Scanning electron microscope (SEM) images of pyrite in the black-and-white banded chert BARB3/111–2130, showing two generations of pyrite, separated by the yellow dashed line. The pyrite cores (first generation) show quartz inclusions (Qz, often spherical shape) and carbonaceous matter (CM, often irregular shape). Numbered white crosses denote the order of analysis spots for sulfur isotope measurements via secondary ion mass spectrometry (SIMS). White crosses in CM indicate the analysis spots for stable carbon isotope analyses. Errors of the $\delta^{13}C_{org}$ values are 2σ estimates (analytical error). **C,** SEM image of pyrite in the black massive chert BARB3/112–2131, showing two generations of pyrite, separated by the yellow dashed lines. The first generation has small phyllosilicate inclusions (Chl, chlorite) and CM (medium-sized black particles). The second generation appears as veins (inside the yellow dashed lines) disrupting the first generation, and exhibits quartz inclusions (Qz, large black clusters). Numbered white crosses denote the order of laser spots for sulfur isotope measurements via SIMS. **D–F,** $\Delta^{33}S$ (black squares) and $\delta^{34}S$ values (orange squares) in transects representing the respective numbered analysis spots marked in pyrites. The error bars represent 2σ errors.

extracts before HyPy (chemical cleaning) do not yield any hydrocarbons or potential precursors such as carboxylic acids (Fig. S4).

3.6. Compound-specific stable carbon isotope analysis

The $\delta^{13}C$ values of individual *n*-alkanes in the 520 °C hydro-pyrolysates of CM from the black-and-white banded cherts range from − 34.1 ± 0.9 ‰ to − 28.3 ± 1.0 ‰, with lowest values detected for BARB3/118–2132 (Fig. 6A, C, D, and Table S4). *n*-Alkanes in the 520 °C hydropyrolysate of CM prepared from the black massive chert (BARB3/112–2131) show $\delta^{13}C$ values between − 29.7 ± 0.2 ‰ and − 27.9 ± 0.2 ‰ (Fig. 6B, and Table S4).

4. Discussion

4.1. Carbonaceous matter in black-and-white banded chert and black massive chert

Carbonaceous matter (CM) frequently appears in all investigated chert samples. Interpretations of the source of the CM in ancient rocks, however, need a sound understanding of the petrographical context and metamorphic history of the material. Many banded cherts of the Buck Reef section evolved from a sediment precursor that formed by direct precipitation of silica from Archean seawater (Ledevin et al., 2019; Lowe and Knauth, 1977; Stefurak et al., 2014, 2015). Some contain abundant
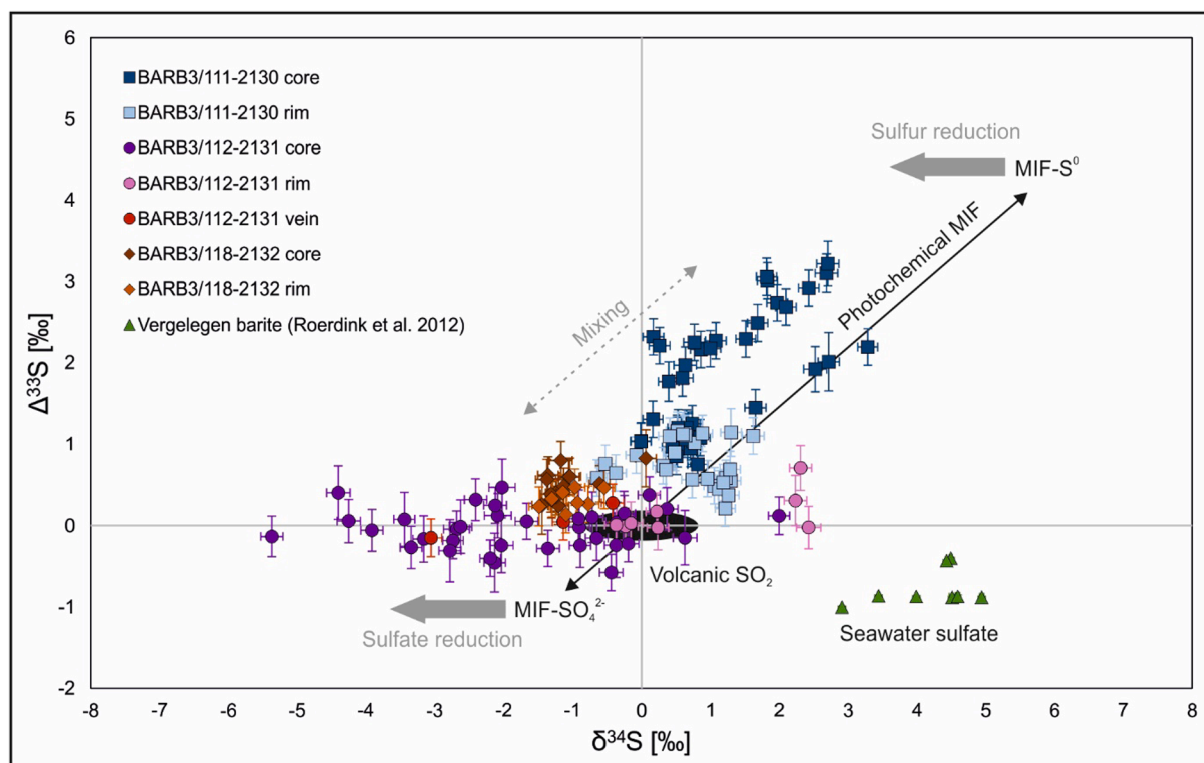
Fig. 5. Microscale sulfur isotope signatures in pyrite. Microscale $\delta^{34}S$ vs. $\Delta^{33}S$ values measured in pyrites from black-and-white banded cherts BARB3/111–2130 (squares, dark blue = core, light blue = rim) and BARB3/118–2132 (diamonds, brown = core, orange = rim), and the black massive chert BARB3/112–2131 (dots, violet = core, pink = rim, red = vein). For comparison, sulfur isotope values of barite from the probably 3.41 Ga old Vergelegen Chert, Barberton greenstone belt (Roerdink et al., 2012), are shown (green triangles), presumably representing the sulfate pool of seawater from that time. The barite-hosting Vergelegen Chert is interpreted to be the westward extension of the Buck Reef Chert (Reimer, 1980). Photochemical reactions in the Archean atmosphere led to mass independent fractionation (MIF) of sulfur from volcanic SO_2 gases, resulting in positive $\Delta^{33}S$ values for sulfur aerosols and negative $\Delta^{33}S$ values for sulfate (Farquhar et al., 2001; Farquhar and Wing, 2003) following the photochemical array (Archean reference array, $\Delta^{33}S/\delta^{34}S \sim 0.73 \pm 0.15$ (Morrison and Mojzsis, 2021; Thomassot et al., 2015)). Pyrite cores from BARB3/111–2130 and BARB3/118–2132 follow a mixing trend between sulfate-derived sulfide with negative $\Delta^{33}S$ and sulfur-derived sulfide with positive $\Delta^{33}S$, which were incorporated into the pyrites in different amounts. Both, microbial and thermochemical sulfur and sulfate reduction shift $\delta^{34}S$ of the produced sulfide to lower values (Machel et al., 1995). All error bars are 2σ estimates. (For interpretation of the references to colour in this figure legend, the reader is referred to the web version of this article.)

primary silica granules, which potentially formed via multi-stage aggregation of silica nano- and microspheres in the water column (Stefurak et al., 2014, 2015). In the three analyzed black-and-white banded cherts, the sedimentary nature is evident by (i) variations of mineralogical composition and CM appearance in distinct layers, (ii) the inclusion of CM in early diagenetic siderite, which likely originates from a ferrous carbonate hydrate precipitate from Archean seawater (Gäb et al., 2017), (iii) the appearance of silica granules and re-worked chert clasts, (iv) the occurrence of rounded detrital carbonaceous grains, and (v) disrupted and rolled-up mat-like structures that indicate soft sediment deformation (Tice and Lowe, 2004, 2006b) (Fig. 3A–G, and Fig. S5). The chert clasts and detrital CM clots indicate a sedimentary regime that was influenced by waves and currents in relatively shallow water (shelf environment above storm wave base (Tice and Lowe, 2006b)), while the appearance of delicate, sediment-draping carbonaceous laminae supports CM formation in microbial biofilms (i.e., microorganisms embedded in organic polymers (Wingender et al., 1999)) covering the former sediment surface. The black massive chert, however, shows none of these features (Fig. 2D, E, and Fig. S5B). Instead, very fine, flattened CM particles together with phyllosilicates indicate a low-energy depositional environment.

While most of the CM in the Buck Reef cherts has a sedimentary context, CM in quartz veins in the form of blocky aggregates or thin films on vein walls and/or in vein centers is secondary (Fig. 3H, I, and Fig. S6). Such CM likely represents pyrobitumen (i.e., once mobile oil, now diagenetically altered and thus, partly insoluble), which provides

evidence for later emplacement of organic matter in the cherts. The Raman spectra of the vein-hosted CM (pyrobitumen) and the sedimentary CM are notably similar, both indicating exposure to lower greenschist-facies conditions around 300 °C, which is in line with previous analyses from the Buck Reef Chert (Alleon et al., 2021; Greco et al., 2018; Hofmann et al., 2013a; Tice et al., 2004; van Zuilen et al., 2007) (Fig. S6, Fig. S7, and Table S2). Hence, the emplacement of mobile pyrobitumen precursors in the cherts must have happened before the regional metamorphic overprint of the Barberton greenstone belt around 3.2 Ga (Cutts et al., 2014). It has been proposed for other cherts from the Buck Reef section that the precursor of the vein-hosted CM (pyrobitumen) may have been released during hydrothermal alteration and migrated only over small distances (Cavalazzi et al., 2021; van Zuilen et al., 2007). The volcanic units capping the Buck Reef Chert do not contain any CM in veins, which further supports that the vein-hosted CM in the studied samples is originating from the Buck Reef Chert itself (van Zuilen et al., 2007). Low H/C ratios ≤ 0.15 (Table 1) provide further support for the Paleoarchean origin of the CM. With increasing metamorphic overprint, the CM typically loses hydrogen due to condensation and aromatization. The analysis via FTIR-ATR, however, revealed that the CM is neither purely graphitic nor completely aromatic, but still has a small aliphatic component (stretching vibrations of aliphatic components at 2956 cm^{-1}, 2924 cm^{-1} and 2851 cm^{-1}; Fig. S8). Hydropyrolysis of the CM released few aliphatic and aromatic hydrocarbons at low concentrations (no more than 9.7 ng/g chert or 11.2 μg/g TOC per compound; Fig. 6, and Table S3), which is in good
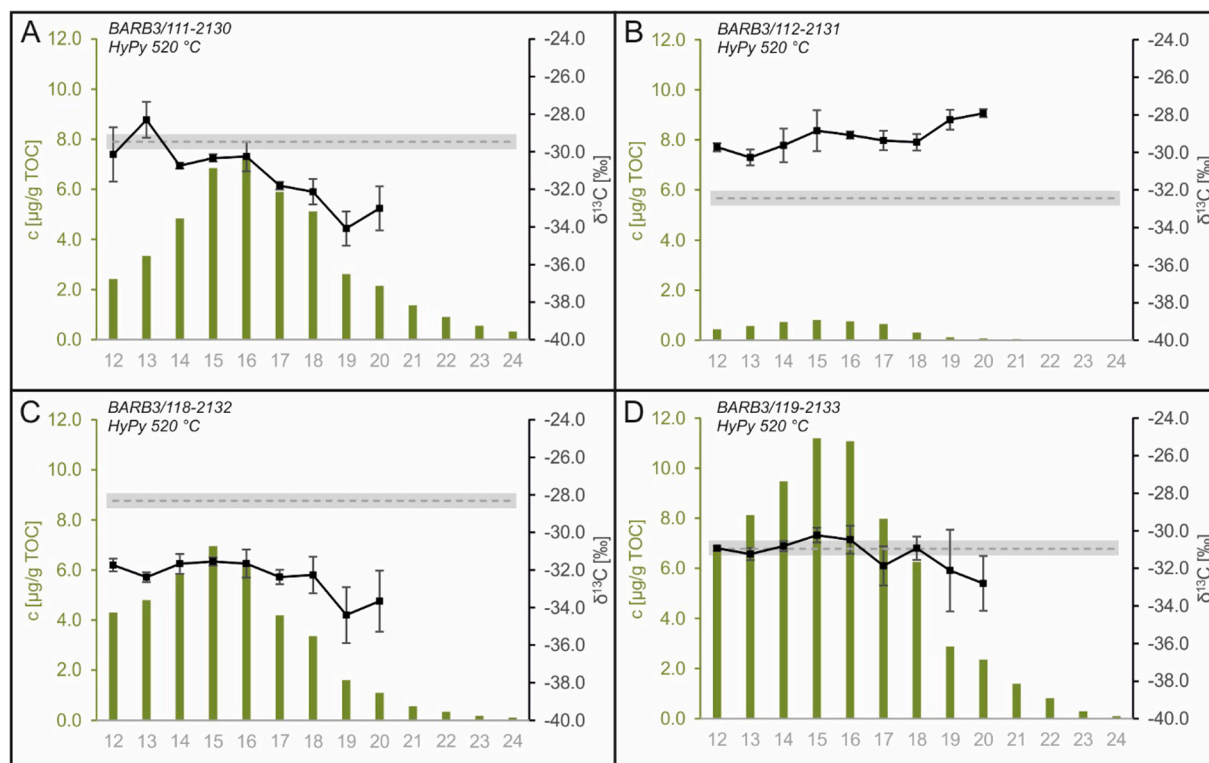
Fig. 6. *n*-Alkanes in 520 °C hydropyrolysates from carbonaceous matter (CM). A–D, Concentrations in μg per g TOC (green bars), and compound specific $\delta^{13}C$ values (black squares) of *n*-alkanes released by 520 °C hydropyrolysis of the extracted CM. Carbon numbers are given on the x-axis. The error bars for compound-specific $\delta^{13}C$ measurements show 2σ estimates. The uncertainty for the concentration data is ≤ 0.1 μg/g TOC. The dashed grey lines represent the $\delta^{13}C_{org}$ values of bulk CM (2σ = ± 0.2 ‰; grey shading).

agreement with (i) the thermal maturity of the CM and (ii) the concentrations reported in other studies for pyrolytically-released hydrocarbons from Archean CM (Duda et al., 2018; French et al., 2015; Marshall et al., 2007). Altogether, the combined results from petrographic, spectroscopic and molecular analyses (incl. Section S1) support that the entire CM pool of the cherts is of Paleoarchean origin.

4.2. Influence of silicification on carbonaceous matter preservation

The conservation of potential traces of life in the rock record is crucial for the reconstruction of early ecosystems. Chert is considered an excellent material for the long-term preservation of biosignatures (McMahon et al., 2018). For instance, early silica cementation has been shown to minimize the degradation of microbial biomass during diagenesis (Alleon et al., 2016). Sedimentary sequences in the Buck Reef Chert show signs of early silicification that promoted the preservation of delicate microbial mat structures and soft sediment deformation features (Hofmann et al., 2013a; Ledevin et al., 2019; Lowe, 1999; Lowe and Knauth, 1977; Stefurak et al., 2014, 2015; Walsh and Lowe, 1999). In the studied samples, rapid silicification, i.e., induration of primary silica precipitates, is evident only in the three black-and-white banded cherts. Notably, primary pyrite crystal cores in these cherts preserved an Archean atmospheric $\Delta^{33}S$ signature ($\Delta^{33}S \neq 0$, here up to 3.2 ± 0.3 ‰; Fig. 4A, B, D, E; Fig. 5). This signature represents a mass independent fractionation (MIF), produced during photochemical reactions of volcanic SO_2 in the Paleoarchean atmosphere (Farquhar et al., 2001; Farquhar and Wing, 2003). Findings of quartz inclusions in these primary pyrites support a silica sediment precursor, while roundish, non-flattened CM particles and delicate mat-like organic laminae (Fig. 3A–F) indicate fast induration of the former sediment before compaction. Occurrences of detrital chert fragments with microbial mat remains in some layers (Fig. 3E, and Fig. S5D) further support the presence of silicified mat horizons at the surface that were available for

intrabasinal re-working.

The black massive chert precursor, on the other hand, probably did not originally contain silica. Rather, the presence of chlorite and sericite replacing earlier clay minerals (Fig. 2D, G), a considerably higher TOC content than in the black-and-white banded cherts (0.5 vs. 0.1 wt%; Table 1), and finely dispersed and flattened CM particles indicate an organic-rich mud precursor. Synsedimentary silicification is not evident. Instead, stratiform veins with quartz, pyrite and phyllosilicates (Fig. 2D–G, and Fig. S6B), and the occurrence of quartz inclusions only in the second pyrite generation (that disrupted the first generation, Fig. 4C, F) indicate that the original sediment was silicified by post-depositional silica impregnation.

The differences in mineralogy and the timing of silicification likely affected the preservation of CM also at the molecular level. Each of the black-and-white banded cherts shows about ten times the yield of pyrolyzable hydrocarbons per gramm TOC compared to the black massive chert (Fig. 6, and Table S3), although all samples experienced the same metamorphic overprint. Presumably, free pore space in the black-and-white-banded cherts was rapidly closed by synsedimentary silicification. Subsequent hydrocarbon migration would therefore have been largely restricted to secondary cracks in the rock matrix. In contrast, the organic mud precursor of the black massive chert provided ample bedding-parallel fluid migration planes for extended periods until it eventually silicified. Hydrocarbons generated from the CM pool during thermal maturation could have easily escaped along those pathways. These processes would have left behind a chemically altered, condensed CM lean in pyrolyzable structural moieties. Such loss of mobile compounds due to delayed silicification is further supported by the slightly heavier $\delta^{13}C$ values of the hydropyrolysis products from the black massive chert CM compared to the black-and-white banded cherts (Fig. 6, and Table S4). This may indicate a more altered CM that had previously lost volatile compounds through thermal maturation. That process would have enriched the remaining carbonaceous residue in ^{13}C

([McKirdy and Powell, 1974](#)).

Notably, in the black massive chert, low *n*-alkane concentrations in the CM hydropyrolysate are accompanied by the absence of carbonaceous structures resembling former biofilms. Biofilms typically have a matrix of extracellular polymeric substances (EPS), biopolymers consisting e.g., of polymerized sugars and proteins that are produced to ensure the structural and functional integrity of the films ([Wingender et al., 1999](#)). During and after the decay of the contained microbial cells, EPS can sequester high-molecular weight alkyl-bearing compounds like phospholipids that were originally stored in the cells ([Wingender et al., 1999](#)), and shield them from immediate recycling. The finely dispersed CM in the black massive chert, on the other hand, may have been derived largely from planktonic primary producers in the water column, where the sinking organic matter was subject to intense degradation during settling and benthic deposition. Therefore, the lower aliphatic hydrocarbon content in the black massive chert CM hydropyrolysate may also be the result of a more refractory parent material.

4.3. Evidence for microbial diversity in the lower platform ecosystem

The record of stable carbon isotopes of sedimentary CM on Earth suggests the presence of autotrophic carbon fixation as early as 3.8 Ga ([Schidlowski, 1988](#)). Photoautotrophs likely dominated the Paleoarchean Buck Reef ecosystem, using the pentose phosphate (Calvin) cycle for carbon fixation and H_2 as the primary reductant ([Tice and Lowe, 2004, 2006a; Walsh and Lowe, 1999](#)). Considering that the carbon pool of Archean oceans and atmosphere was substantially

influenced by mantle outgassing ([Des Marais, 1985](#)), with mantle carbon having a $\delta^{13}C$ between -8 and -3 ‰ ([Deines and Gold, 1973; Des Marais, 2001; Des Marais and Moore, 1984; Schidlowski, 1988](#)), the $\delta^{13}C_{org}$ values of bulk CM in the studied cherts between -32.4 ± 0.2 ‰ and -28.3 ± 0.2 ‰, and of the pyrolytically released *n*-alkanes between -34.1 ± 0.9 ‰ and -27.9 ± 0.2 ‰ ([Fig. 6, Fig. 7, Table 1](#), and [Table S4](#)) are consistent with carbon fixation via the Calvin cycle ([House et al., 2003; Pearson, 2010; Schidlowski, 1988](#)).

Local CM accumulations in two black-and-white banded cherts, however, are depleted in ^{13}C, with pyrite-associated CM in BARB3/111–2130 and siderite-associated CM in BARB3/118–2132 showing $\delta^{13}C_{org}$ values as low as -39.9 ± 0.3 ‰ and -44.0 ± 0.9 ‰, respectively ([Fig. 3G, Fig. 4B, Fig. 7](#), and [Table 1](#)). These values cannot be explained by carbon fixation via the Calvin cycle. Some chemoautotrophic sulfate reducing bacteria that use the acetyl coenzyme A (acetyl-CoA) pathway for carbon fixation can discriminate stronger against ^{13}C (-36 ‰) ([Preuß et al., 1989](#)), which may plausibly explain the $\delta^{13}C_{org}$ values in pyrite CM from BARB3/111–2130 ([Fig. 4B](#)). The former presence of sulfate reducers is also in agreement with the $\Delta^{33}S$ profile of pyrite cores in that sample. This profile can be interpreted as a mixing line ([Fig. 5](#)) retracing contributions of both, photolytic sulfate-derived sulfide with negative $\Delta^{33}S$ and photolytic elemental sulfur-derived sulfide with positive $\Delta^{33}S$ ([Lyons, 2009](#)). The environmental influence of sulfate reducing microbes, however, was likely not substantial, as $\Delta^{33}S > 1$ ‰ ([Fig. 5](#)) suggest that the main sulfur source for pyrite formation was elemental sulfur not sulfate ([Farquhar et al., 2001; Farquhar and Wing, 2003](#)), and sulfate concentrations in Archean sea water were
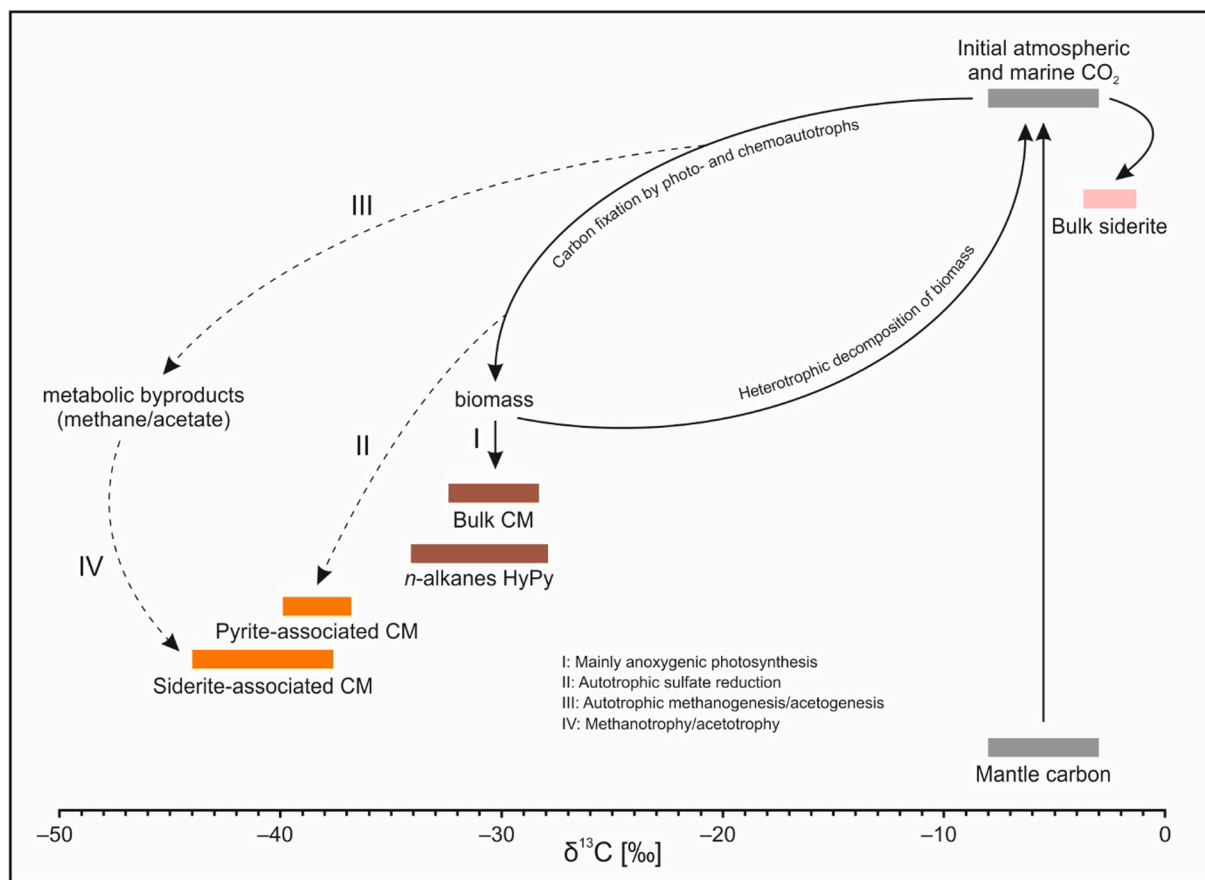

Fig. 7. Schematic compilation of carbon isotope data and inferred carbon cycle processes in the lower platform environment (Buck Reef Chert). Photo- and chemoautotrophs likely dominated the lower platform ecosystem (I) as indicated by low $\delta^{13}C_{org}$ values of bulk CM and pyrolytic *n*-alkanes (brown boxes). Autotrophic sulfate reducers (II) and methanogen-methanotroph or acetogen-acetotroph couples (III, IV) locally thrived under particular environmental conditions. This is evidenced in two samples by strongly ^{13}C-depleted CM in association with pyrite and siderite (orange boxes). Heterotrophic decomposition of biomass and/or methanotrophs/acetotrophs returned isotopically light carbon to the dissolved marine inorganic carbon pool. This is indicated by the small offset between the $\delta^{13}C_{carb}$ values of siderite (i.e., bulk carbonate; pink box) and the marine carbon reservoir (grey boxes) from which the siderite precursor precipitated.

likely low (Habicht et al., 2002). The small variations in $\delta^{34}S$ (Fig. 5) can theoretically be caused by thermochemical sulfate reduction (Machel et al., 1995), but are also consistent with microbial sulfate reduction under low sulfate concentrations (Habicht et al., 2002).

The acetyl-CoA pathway is considered as one of the most primitive metabolisms (Fuchs, 2011), and is also used e.g., by some methanogens and acetogens (Fuchs and Stupperich, 1982; House et al., 2003) that both produce strongly ^{13}C-depleted metabolic products (methane and acetate, respectively) (Botz et al., 1996; Gelwicks et al., 1989; Pearson, 2010). Microbial consumption of these molecules by methanotrophs or acetotrophs typically incorporates the ^{13}C-depleted carbon into their biomass (Pearson, 2010), which could plausibly explain the substantially ^{13}C-depleted CM that locally occurs in BARB3/118–2132. If so, it seems that such methanogenesis-methanotrophy or acetogenesis-acetotrophy couples became abundant only under particular environmental conditions, as the strongly ^{13}C-depleted CM is only observed in a certain layer in association with siderite (Fig. 3G).

The siderite in the sedimentary layers is probably a diagenetic product of a ferrous carbonate hydrate precipitate from Archean seawater (Gäb et al., 2017), because secondary formation via Fe(III)-reduction is not evident (Tice and Lowe, 2004, 2006a, b). The bulk $\delta^{13}C_{carb}$ values of the siderite carbon range between -3.7 ± 0.2 ‰ and -1.3 ± 0.2 ‰ (Table 1) and thus are close to the $\delta^{13}C$ of the initial inorganic carbon pool of Archean seawater (Fig. 7; Des Marais, 2001). This can be explained by an input of isotopically light carbon from heterotrophic decomposition of biomass and/or methanotrophy/acetotrophy to the dissolved inorganic carbon pool from which the siderite precursor precipitated (otherwise the siderite should become more ^{13}C-enriched). Heterotrophy can hardly be traced in the stable carbon isotope record of CM, as the $\delta^{13}C_{org}$ of biomass from heterotrophs is close to the $\delta^{13}C_{org}$ of the diet (DeNiro and Epstein, 1978; Pearson, 2010). However, a heterotrophic lifestyle likely was important in Paleoarchean ecosystems, given that the consumption of organic carbon (including meteoritic carbon) is metabolically simple and therefore considered one of the most ancient metabolisms (Oparin, 1938).

Abiotic synthesis processes, such as Fischer-Tropsch-type (FTT) reactions, can also produce organic compounds strongly depleted in ^{13}C (McCollom and Seewald, 2006). However, the $\delta^{13}C_{org}$ of abiotic organic molecules formed experimentally under hydrothermal conditions and of abiotic CM found in Archean serpentinites varies only by a few per mill (Hofmann and Bolhar, 2007; McCollom and Seewald, 2006). For our samples with strongly varying $\delta^{13}C_{org}$ values of CM, we therefore consider the contribution of such abiotic CM as unlikely. Second, the Buck Reef Chert is not underlain by ultramafic rocks, which upon serpentinization could have resulted in abiotic hydrocarbon generation. Instead, it is underlain by a thick pile of felsic volcanic rocks, making an abiotic pathway for reduced C-compounds via FTT reactions impossible (Hofmann and Bolhar, 2007). Likewise, the black-and-white banded cherts do not show features of intensive hydrothermal alteration, and the geochemical biosignatures are found together with microbial mat structures.

Other sections of the Buck Reef Chert provide additional evidence for the existence of microbial metabolisms. Anaerobic ammonium oxidation was recorded especially in the upper part of the section (Pellerin et al., 2023), while methane metabolizing microbes likely colonized a hydrothermal chert vein system in stratigraphic continuity to the Buck Reef Chert (Cavalazzi et al., 2021). Thus, the Buck Reef Chert preserved one of the most diverse microbial ecosystems known from the Paleoarchean. Microbial diversity was also reported from other Paleoarchean environments (Hickman-Lewis et al., 2020b; Morag et al., 2016; Westall et al., 2011), underlining that complex microbial ecosystems were already widely established during these early times.

5. Conclusions

Four carbonaceous cherts from the lower platform facies of the ca.

3.42 Ga old Buck Reef Chert, Barberton greenstone belt, were investigated on multiple scales. CM frequently appears in the cherts and mainly originates from Paleoarchean biomass. The timing of silicification of the cherts influenced the preservation of the CM; a higher pyrolysis yield of hydrocarbons was observed in the cherts that were rapidly silicified. Geochemical analyses, including microscale stable carbon isotopes of the CM and multiple sulfur isotopes of pyrite, indicate that the lower platform ecosystem of the Buck Reef Chert temporarily hosted complex microbial communities. These communities likely consisted of photo-autotrophs, autotrophic sulfate reducers and methane- or acetate-producing microbes. Methanotrophs or acetotrophs may also have contributed to the overall biomass. These results highlight the existence of an advanced biological carbon cycle as early as 3.42 Ga ago.

Declaration of competing interest

The authors declare that they have no known competing financial interests or personal relationships that could have appeared to influence the work reported in this paper.

Data availability

Data will be made available on request.

1450/3-1 and 1450/3-2 to JPD, and Re 665/42-2 to JR), and the Lower Saxony Government program "Research Cooperation with Foreign Countries" (travel support for JR and JPD).

Appendix A. Supplementary material

Supplementary data to this article can be found online at https://doi.org/10.1016/j.precamres.2024.107289.

References

Alleon, J., Bernard, S., Le Guillou, C., Daval, D., Skouri-Panet, F., Pont, S., Delbes, L., Robert, F., 2016. Early entombment within silica minimizes the molecular degradation of microorganisms during advanced diagenesis. Chem. Geol. 437, 98–108.

Alleon, J., Bernard, S., Olivier, N., Thomazo, C., Marin-Carbonne, J., 2021. Inherited geochemical diversity of 3.4 Ga organic films from the Buck Reef Chert, South Africa. Commun. Earth Environ. 2, 6.

Beyssac, O., Goffé, B., Chopin, C., Rouzaud, J.N., 2002. Raman spectra of carbonaceous material in metasediments: a new geothermometer. J. Metam. Geol. 20, 859–871.

Botz, R., Pokojski, H.-D., Schmitt, M., Thomm, M., 1996. Carbon isotope fractionation during bacterial methanogenesis by CO_2 reduction. Org. Geochem. 25, 255–262.

Brasier, M.D., Green, O.R., Jephcoat, A.P., Kleppe, A.K., Van Kranendonk, M.J., Lindsay, J.F., Steele, A., Grassineau, N.V., 2002. Questioning the evidence for Earth's oldest fossils. Nature 416, 76–81.

Brocks, J.J., Love, G.D., Snape, C.E., Logan, G.A., Summons, R.E., Buick, R., 2003. Release of bound aromatic hydrocarbons from late Archean and Mesoproterozoic kerogens via hydropyrolysis. Geochim. Cosmochim. Acta 67, 1521–1530.

Cabral, R.A., Jackson, M.G., Rose-Koga, E.F., Koga, K.T., Whitehouse, M.J., Antonelli, M. A., Farquhar, J., Day, J.M.D., Hauri, E.H., 2013. Anomalous sulphur isotopes in plume lavas reveal deep mantle storage of Archaean crust. Nature 496, 490–493.

Cavalazzi, B., Lemelle, L., Simionovici, A., Cady, S.L., Russell, M.J., Bailo, E., Canteri, R., Enrico, E., Manceau, A., Maris, A., Salomé, M., Thomassot, E., Bouden, N., Tucoulou, R., Hofmann, A., 2021. Cellular remains in a ~3.42-billion-year-old subseafloor hydrothermal environment. Sci. Adv. 7.

Crowe, D.E., Vaughan, R.G., 1966. Characterization and use of isotopically homogeneous standards for in situ laser microprobe analysis of $^{34}S/^{32}S$ ratios. Am. Mineral. 81, 187–193.

Cutts, K.A., Stevens, G., Hoffmann, J.E., Buick, I.S., Frei, D., Münker, C., 2014. Paleo- to Mesoarchean polymetamorphism in the Barberton Granite-Greenstone Belt, South Africa: Constraints from U-Pb monazite and Lu-Hf garnet geochronology on the tectonic processes that shaped the belt GSA. Bulletin 126, 251–270.

Deines, P., Gold, D.P., 1973. The isotopic composition of carbonatite and kimberlite carbonates and their bearing on the isotopic composition of deep-seated carbon. Geochim. Cosmochim. Acta 37, 1709–1733.

DeNiro, M.J., Epstein, S., 1978. Influence of diet on the distribution of carbon isotopes in animals. Geochim. Cosmochim. Acta 42, 495–506.

Des Marais, D.J., 1985. Carbon exchange between the mantle and the crust, and its effect upon the atmosphere: Today compared to archean time. In: Sundquist, E.T., Broecker, W.S. (Eds.), The Carbon Cycle and Atmospheric CO_2: Natural Variations Archean to Present. American Geophysical Union.

Des Marais, D.J., 2001. Isotopic evolution of the biogeochemical carbon cycle during the precambrian. Rev. Mineral. Geochem. 43, 555–578.

Des Marais, D.J., Moore, J.G., 1984. Carbon and its isotopes in mid-oceanic basaltic glasses. Earth Planet. Sci. Lett. 69, 43–57.

Djokic, T., Van Kranendonk, M.J., Campbell, K.A., Walter, M.R., Ward, C.R., 2017. Earliest signs of life on land preserved in ca. 3.5 Ga hot spring deposits. Nat. Commun. 8, 15263.

Duda, J.-P., Thiel, V., Bauersachs, T., Mißbach, H., Reinhardt, M., Schäfer, N., Van Kranendonk, M.J., Reitner, J., 2018. Ideas and perspectives: hydrothermally driven redistribution and sequestration of early Archaean biomass – the "hydrothermal pump hypothesis". Biogeosciences 15, 1535–1548.

Durand, B., 1980. Sedimentary organic matter and kerogen. Definition and quantitative importance of kerogen. In: Durand, B. (Ed.), Kerogen: Insoluble Organic Matter from Sedimentary Rocks. Editions Technip, Paris, pp. 13–34.

Farquhar, J., Savarino, J., Airieau, S., Thiemens, M.H., 2001. Observation of wavelength-sensitive mass-independent sulfur isotope effects during SO_2 photolysis: Implications for the early atmosphere. JGR Planets 106, 32829–32839.

Farquhar, J., Wing, B.A., 2003. Multiple sulfur isotopes and the evolution of the atmosphere. Earth Planet. Sci. Lett. 213, 1–13.

Fernandez, A., van Dijk, J., Müller, I.A., Bernasconi, S.M., 2016. Siderite acid fractionation factors for sealed and open vessel digestions at 70 °C and 100 °C. Chem. Geol. 444, 180–186.

French, K.L., Hallmann, C., Hope, J.M., Schoon, P.L., Zumberge, J.A., Hoshino, Y., Peters, C.A., George, S.C., Love, G.D., Brocks, J.J., Buick, R., Summons, R.E., 2015. Reappraisal of hydrocarbon biomarkers in Archean rocks. PNAS 112, 5915–5920.

Fuchs, G., 2011. Alternative pathways of carbon dioxide fixation: Insights into the early evolution of life? Annu. Rev. Microbiol. 65, 631–658.

Fuchs, G., Stupperich, E., 1982. Autotrophic CO_2 Fixation Pathway in Methanobacterium thermoautotrophicum. Zentralblatt für Bakteriologie Mikrobiologie und Hygiene: I. Abt. Originale C: Allgemeine. Angew. Ökolog. Mikrobiol. 3, 277–288.

Gäb, F., Ballhaus, C., Siemens, J., Heuser, A., Lissner, M., Geisler, T., Garbe-Schönberg, D., 2017. Siderite cannot be used as CO_2 sensor for Archaean atmospheres. Geochim. Cosmochim. Acta 214, 209–225.

Gelwicks, J.T., Risatti, J.B., Hayes, J.M., 1989. Carbon isotope effects associated with autotrophic acetogenesis. Org. Geochem. 14, 441–446.

Greco, F., Cavalazzi, B., Hofmann, A., Hickman-Lewis, K., 2018. 3.4 Ga biostructures from the Barberton greenstone belt of South Africa: new insights into microbial life. Boll. Soc. Paleontol. Italiana 57, 59–74.

Habicht, K.S., Gade, M., Thamdrup, B., Berg, P., Canfield, D.E., 2002. Calibration of sulfate levels in the archean ocean. Science 298, 2372–2374.

Hickman-Lewis, K., Cavalazzi, B., Foucher, F., Westall, F., 2018. Most ancient evidence for life in the Barberton greenstone belt: Microbial mats and biofabrics of the ~3.47 Ga Middle Marker horizon. Precambr. Res. 312, 45–67.

Hickman-Lewis, K., Cavalazzi, B., Sorieul, S., Gautret, P., Foucher, F., Whitehouse, M.J., Jeon, H., Georgelin, T., Cockell, C.S., Westall, F., 2020a. Metallomics in deep time and the influence of ocean chemistry on the metabolic landscapes of Earth's earliest ecosystems. Sci. Rep. 10, 4965.

Hickman-Lewis, K., Westall, F., Cavalazzi, B., 2020b. Diverse communities of Bacteria and Archaea flourished in Palaeoarchaean (3.5–3.3 Ga) microbial mats. Palaeontology 63, 1007–1033.

Hofmann, A., Bolhar, R., 2007. Carbonaceous cherts in the barberton greenstone belt and their significance for the study of early life in the archean record. Astrobiology 7, 355–388.

Hofmann, A., Bolhar, R., Orberger, B., Foucher, F., 2013a. Cherts of the Barberton Greenstone Belt, South Africa: Petrology and trace-element geochemistry of 3.5 to 3.3 Ga old silicified volcaniclastic sediments. S. Afr. J. Geol. 116, 297–322.

Hofmann, A., Karykowski, B., Mason, P., Chunnet, G., Arndt, N., 2013b. Barberton drilling project – Buck Reef Chert core BARB3. EGU General Assembly, Vienna.

Homann, M., 2019. Earliest life on Earth: Evidence from the Barberton Greenstone Belt, South Africa. Earth-Sci. Rev. 196, 102888.

House, C.H., Schopf, J.W., McKeegan, K.D., Coath, C.D., Harrison, T.M., Stetter, K.O., 2000. Carbon isotopic composition of individual Precambrian microfossils. Geology 28, 707–710.

House, C.H., Schopf, J.W., Stetter, K.O., 2003. Carbon isotopic fractionation by Archaeans and other thermophilic prokaryotes. Org. Geochem. 34, 345–356.

Ledevin, M., Arndt, N., Chauvel, C., Jaillard, E., Simionovici, A., 2019. The Sedimentary Origin of Black and White Banded Cherts of the Buck Reef, Barberton, South Africa. Geosciences 9, 424.

Lepot, K., 2020. Signatures of early microbial life from the Archean (4 to 2.5 Ga) eon. Earth Sci. Rev. 209, 103296.

Love, G.D., Snape, C.E., Carr, A.D., Houghton, R.C., 1995. Release of covalently-bound alkane biomarkers in high yields from kerogen via catalytic hydropyrolysis. Org. Geochem. 23, 981–986.

Love, A.H., 1982. Kerogen-isolation method - a study with kerogen data from sedimentary rocks.

Lowe, D.R., 1999. Petrology and sedimentology of cherts and related silicified sedimentary rocks in the Swaziland Supergroup. In: Lowe, D.R., Byerly, G.R. (Eds.), Geologic Evolution of the Barberton Greenstone Belt, South Africa. Geological Society of America, Boulder, Colorado.

Lowe, D.R., Fisher Worrell, G., 1999. Sedimentology, mineralogy, and implications of silicified evaporites in the Kromberg Formation, Barberton Greenstone Belt, South Africa, in: Lowe, D.R., Byerly, G.R. (Eds.), Geologic Evolution of the Barberton Greenstone Belt, South Africa. Geological Society of America Special Paper 329, Boulder, Colorado, pp. 167–188.

Lowe, D.R., Knauth, L.P., 1977. Sedimentology of the Onverwacht Group (3.4 Billion Years), Transvaal, South Africa, and Its Bearing on the Characteristics and Evolution of the Early Earth. J. Geol. 85, 699–723.

Lyons, J.R., 2009. Atmospherically-derived mass-independent sulfur isotope signatures, and incorporation into sediments. Chem. Geol. 267, 164–174.

Machel, H.G., Krouse, H.R., Sassen, R., 1995. Products and distinguishing criteria of bacterial and thermochemical sulfate reduction. Appl. Geochem. 10, 373–389.

Magnall, J.M., Gleeson, S.A., Stern, R.A., Newton, R.J., Poulton, S.W., Paradis, S., 2016. Open system sulphate reduction in a diagenetic environment – Isotopic analysis of barite ($\delta^{34}S$ and $\delta^{18}O$) and pyrite ($\delta^{34}S$) from the Tom and Jason Late Devonian Zn–Pb–Ba deposits, Selwyn Basin, Canada. Geochim. Cosmochim. Acta 180, 146–163.

Marshall, C.P., Love, G.D., Snape, C.E., Hill, A.C., Allwood, A.C., Walter, M.R., Van Kranendonk, M.J., Bowden, S.A., Sylva, S.P., Summons, R.E., 2007. Structural characterization of kerogen in 3.4 Ga Archaean cherts from the Pilbara Craton, Western Australia. Precambr. Res. 155, 1–23.

McCollom, T.M., Seewald, J.S., 2006. Carbon isotope composition of organic compounds produced by abiotic synthesis under hydrothermal conditions. Earth Planet. Sci. Lett. 243, 74–84.

McKirdy, D.M., Powell, T.G., 1974. Metamorphic Alteration of Carbon Isotopic Composition in Ancient Sedimentary Organic Matter: New Evidence from Australia and South Africa. Geology 2, 591–595.

McMahon, S., 2019. Earth's earliest and deepest purported fossils may be iron-mineralized chemical gardens. Proc. R. Soc. B 286, 20192410.

McMahon, S., Bosak, T., Grotzinger, J.P., Milliken, R.E., Summons, R.E., Daye, M., Newman, S.A., Fraeman, A., Williford, K.H., Briggs, D.E.G., 2018. A field guide to finding fossils on mars. JGR Planets 123, 1012–1040.

Meredith, W., Russell, C.A., Cooper, M., Snape, C.E., Love, G.D., Fabbri, D., Vane, C.H., 2004. Trapping hydropyrolysates on silica and their subsequent thermal desorption to facilitate rapid fingerprinting by GC–MS. Org. Geochem. 35, 73–89.

Morag, N., Williford, K.H., Kitajima, K., Philippot, P., Van Kranendonk, M.J., Lepot, K., Thomazo, C., Valley, J.W., 2016. Microstructure-specific carbon isotopic signatures

of organic matter from ~3.5 Ga cherts of the Pilbara Craton support a biologic origin. Precambr. Res. 275, 429–449.

Morrison, P.R., Mojzsis, S.J., 2021. Tracing the early emergence of microbial sulfur metabolisms. Geomicrobiol J. 38, 66–86.

Nemchin, A., Whitehouse, M.J., Menneken, M., Geisler, T., Pidgeon, R.T., Wilde, S.A., 2008. A light carbon reservoir recorded in zircon-hosted diamond from the Jack Hills. Nature 454, 92–95.

Oparin, A.I., 1938. The origin of life. Macmillan, New York.

Pearson, A., 2010. Pathways of carbon assimilation and their impact on organic matter values δ^{13}C. In: Timmis, K.N. (Ed.), Handbook of Hydrocarbon and Lipid Microbiology. Springer, Berlin.

Pellerin, A., Thomazo, C., Ader, M., Marin-Carbonne, J., Alleon, J., Vennin, E., Hofmann, A., 2023. Iron-mediated anaerobic ammonium oxidation recorded in the early Archean ferruginous ocean. Geobiology 00, 1–13.

Philippot, P., Van Zuilen, M.A., Lepot, K., Thomazo, C., Farquhar, J., Van Kranendonk, M.J., 2007. Early archaean microorganisms preferred elemental sulfur, not sulfate. Science 317, 1534–1537.

Preuß, A., Schauder, R., Fuchs, G., Stichler, W., 1989. Carbon isotope fractionation by autotrophic bacteria with three different CO_2 fixation pathways. Z. Naturforschung C.

Reimer, T.O., 1980. Archean sedimentary baryte deposits of the Swaziland Supergroup (Barberton Mountain Land, South Africa). Precambr. Res. 12, 393–410.

Reinhardt, M., Goetz, W., Duda, J.-P., Heim, C., Reitner, J., Thiel, V., 2019. Organic signatures in Pleistocene cherts from Lake Magadi (Kenya) – implications for early Earth hydrothermal deposits. Biogeosciences 16, 2443–2465.

Roerdink, D.L., Mason, P.R.D., Farquhar, J., Reimer, T.O., 2012. Multiple sulfur isotopes in Paleoarchean barites identify an important role for microbial sulfate reduction in the early marine environment. Earth Planet. Sci. Lett. 331–332, 177–186.

Sangély, L., Chaussidon, M., Michels, R., Huault, V., 2005. Microanalysis of carbon isotope composition in organic matter by secondary ion mass spectrometry. Chem. Geol. 223, 179–195.

Schidlowski, M., 1988. A 3,800-million-year isotopic record of life from carbon in sedimentary rocks. Nature 333, 313–318.

Sforna, M.C., van Zuilen, M.A., Philippot, P., 2014. Structural characterization by Raman hyperspectral mapping of organic carbon in the 3.46 billion-year-old Apex chert, Western Australia. Geochim. Cosmochi. Acta 124, 18–33.

Stefurak, E.J.T., Lowe, D.R., Zentner, D., Fischer, W.W., 2014. Primary silica granules—A new mode of Paleoarchean sedimentation. Geology 42, 283–286.

Stefurak, E.J.T., Lowe, D.R., Zentner, D., Fischer, W.W., 2015. Sedimentology and geochemistry of Archean silica granules. GSA Bull. 127, 1090–1107.

Thomassot, E., O'Neil, J., Francis, D., Cartigny, P., Wing, B.A., 2015. Atmospheric record in the Hadean Eon from multiple sulfur isotope measurements in Nuvvuagittuq Greenstone Belt (Nunavik, Quebec). PNAS 112, 707–712.

Tice, M.M., 2009. Environmental Controls on Photosynthetic Microbial Mat Distribution and Morphogenesis on a 3.42 Ga Clastic-Starved Platform. Astrobiology 9, 989–1000.

Tice, M.M., Bostick, B.C., Lowe, D.R., 2004. Thermal history of the 3.5–3.2 Ga Onverwacht and Fig Tree Groups, Barberton greenstone belt, South Africa, inferred by Raman microspectroscopy of carbonaceous material. Geology 32, 37–40.

Tice, M.M., Lowe, D.R., 2004. Photosynthetic microbial mats in the 3,416-Myr-old ocean. Nature 431, 549–552.

Tice, M.M., Lowe, D.R., 2006a. Hydrogen-based carbon fixation in the earliest known photosynthetic organisms. Geology 34, 37–40.

Tice, M.M., Lowe, D.R., 2006b. The origin of carbonaceous matter in pre-3.0 Ga greenstone terrains: A review and new evidence from the 3.42 Ga Buck Reef Chert. Earth Sci. Rev. 76, 259–300.

Ueno, Y., Yamada, K., Yoshida, N., Maruyama, S., Isozaki, Y., 2006. Evidence from fluid inclusions for microbial methanogenesis in the early Archaean era. Nature 440.

van Zuilen, M.A., Chaussidon, M., Rollion-Bard, C., Marty, B., 2007. Carbonaceous cherts of the Barberton Greenstone Belt, South Africa: Isotopic, chemical and structural characteristics of individual microstructures. Geochim. Cosmochim. Acta 71, 655–669.

Wacey, D., McLoughlin, N., Whitehouse, M.J., Kilbrun, M.R., 2010. Two coexisting sulfur metabolisms in a ca. 3400 Ma sandstone. Geology 38, 1115–1118.

Walsh, M.M., Lowe, D.R., 1985. Filamentous microfossils from the 3,500-Myr-old Onverwacht Group, Barberton Mountain Land, South Africa. Nature 314, 530–532.

Walsh, M.M., Lowe, D.R., 1999. Modes of accumulation of carbonaceous matter in the early Archean: A petrographic and geochemical study of the carbonaceous cherts of the Swaziland Supergroup. In: Lowe, D.R., Byerly, G.R. (Eds.), Geologic Evolution of the Barberton Greenstone Belt, South Africa. Geological Society of America, Boulder, Colorado.

Welin, E., 1966. The Occurrence of Asphaltite and Thucholite in the Precambrian Bedrock of Sweden. Geologiska Föreningen i Stockholm Förhandlingar 87, 509–526.

Westall, F., Cavalazzi, B., Lemelle, L., Marrocchi, Y., Rouzaud, J.N., Simionovici, A., Salomé, M., Mostefaoui, S., Andreazza, C., Foucher, F., Toporski, J.K.W., Jauss, A., Thiel, V., Southam, G., MacLean, L., Wirick, S., Hofmann, A., Meibom, A., Robert, F., Défarge, C., 2011. Implications of in situ calcification for photosynthesis in a ~ 3.3 Ga-old microbial biofilm from the Barberton greenstone belt, South Africa. Earth Planet. Sci. Lett. 310, 468–479.

Whitehouse, M.J., 2013. Multiple sulfur isotope determination by SIMS: Evaluation of reference sulfides for Δ^{33}S with observations and a case study on the determination of Δ^{36}S. Geostand. Geoanal. Res. 37, 19–33.

Wingender, J., Neu, T.R., Flemming, H.-C., 1999. What are Bacterial Extracellular Polymeric Substances?, in: Wingender, J., Neu, T.R., Flemming, H.-C. (Eds.), Microbial Extracellular Polymeric Substances Springer, Berlin, p. 258.